

**İZMİR KATIP CELEBI UNIVERSITY
GRADUATE SCHOOL OF NATURAL AND APPLIED SCIENCES**

**BIOMECHANICS OF ACETABULAR FRACTURES WITH LOW ENERGY
TRAUMA VIA FINITE ELEMENT MODELING AND ANALYSIS**



M.Sc. THESIS

Samet ÇIKLAÇANDIR

Department of Biomedical Technologies

JANUARY 2019

**IZMIR KATIP CELEBI UNIVERSITY
GRADUATE SCHOOL OF NATURAL AND APPLIED SCIENCES**

**BIOMECHANICS OF ACETABULAR FRACTURES WITH LOW ENERGY
TRAUMA VIA FINITE ELEMENT MODELING AND ANALYSIS**



M.Sc. THESIS

**Samet ÇIKLAÇANDIR
(Y160204010)**

Department of Biomedical Technologies

**Thesis Advisor: Yalçın İŞLER,
Thesis Co-Advisor: Şenay MİHÇİN**

JANUARY 2019

İZMİR KATİP ÇELEBİ ÜNİVERSİTESİ
FEN BİLİMLERİ ENSTİTÜSÜ

DÜŞÜK ENERJİ TRAVMALI ACETABULAR KIRIKLARININ SONLU
ELEMANLAR MODELİ VE ANALİZİ

YÜKSEK LİSANS

Samet ÇIKLAÇANDIR
(Y160204010)

Biyomedikal Teknolojileri Ana Bilim Dalı

Tez Danışmanı: Yalçın İŞLER,
Tez Eş Danışmanı: Şenay MİHÇİN

OCAK 2019

Samet IKLAÇANDIR, a **M.Sc.** student of **IKCU Graduate School Of Natural And Applied Sciences**, successfully defended the thesis entitled “**BIOMECHANICS OF ACETABULAR FRACTURES WITH LOW ENERGY TRAUMA VIA FINITE ELEMENT MODELING AND ANALYSIS**”, which he prepared after fulfilling the requirements specified in the associated legislations, before the jury whose signatures are below.

Thesis Advisor :

Asst. Prof. Dr. Yalçın İşler
İzmir Katip Çelebi University

Thesis Co-Advisor :

Asst. Prof. Dr. Şenay Mihçin
İzmir Katip Çelebi University

Jury Members :

Assoc. Prof. Dr. Yakup Kutlu
İskenderun Technical University

Asst. Prof. Dr. Yılmaz Kemal Yüce
Alanya Alaaddin Keykubat University

Asst. Prof. Dr. Nalan Özkurt
Yaşar University

Date of Submission : 19.12.2018

Date of Defense : 07.01.2019



To my family,

FOREWORD

I would like to thank many people for their help in this very intensive study. First of all, I would like to express my gratitude to Asst. Prof. Dr. Yalçın İşler. He has always supported my thesis study and has helped with many things. Especially, he directed me to the Erasmus Programme so that he enabled me to learn many things there. I would like to thank my thesis co-supervisor Asst. Prof. Dr. Şenay Mihçin, who helped me with many things that I struggled with. I am grateful to my advisors who have inspired me with their vision and hard work. In addition, I want to express my gratitude for our head of the department, Prof. Dr. Aydın Akan, who has always supported our department and followed our personal development by guiding us. I also would like to thank Prof. Dr. Timo Jämsä, who is my advisor during the Erasmus at Oulu University, for his interest and patience. Finally, I am very grateful to my friend Abdulwahed Kajabi who has always been with me in the Erasmus for his valuable comments and revisions of the manuscript.

Of course, I would like to express my warmest gratitude to my dear family, especially my wife, for their love and support throughout my life.

January 2019

Samet ÇIKLAÇANDIR

TABLE OF CONTENTS

	<u>Page</u>
FOREWORD	ix
TABLE OF CONTENTS	xi
ABBREVIATIONS	xiii
LIST OF TABLES	xv
LIST OF FIGURES	xvii
ABSTRACT	xix
ÖZET	xxi
1. INTRODUCTION	1
2. LITERATURE REVIEW	5
2.1 Bone - A brief anatomical review	6
2.2 Acetabular fracture types.....	8
2.3 Imaging Methods.....	9
2.4 Finite Element Method.....	9
3. MATERIALS AND METHODS	15
3.1 Subjects	15
3.2 Image Segmentation.....	16
3.3 Meshing.....	19
3.4 Material Properties	20
3.5 Boundary Conditions.....	30
3.6 Boundary Conditions: Loading	30
3.7 Cortical Thickness.....	31
4. RESULTS	33
5. DISCUSSION	43
6. CONCLUSIONS	45
REFERENCES	47
APPENDIX	53
CURRICULUM VITAE	55



ABBREVIATIONS

3D	: 3-Dimensional
Δ	: Difference of Two Values
ε	: Strain
ρ_{app}	: Computed Tomography Density
σ	: Stress
σ_{VM}	: Von Mises Stress
BMD	: Bone Mineral Density
BMI	: Body Mass Index
E	: Young's Modulus
F	: Nodal Force
FE	: Finite Element
FEA	: Finite Element Analysis
FEM	: Finite Element Modeling
HU	: Hounsfield Unit
K	: Stiffness Matrix
CT	: Computed Tomography
MDCT	: Multiple Detector Computed Tomography
QCT	: Quantitative Computed Tomography
U	: Global Nodal Displacement
MRI	: Magnetic Resonance Imaging
DXA	: Dual-Energy X-ray Absorptiometry



LIST OF TABLES

	<u>Page</u>
Table 3.1 : The number of nodes and the number of elements for each model.	20
Table 3.2: Max, Min and Average of the density and E-Modulus of the left femur model with an acetabular fracture	22
Table 3.3: Max, Min and Average of the density and E-Modulus of the left pelvic model with an acetabular fracture	23
Table 3.4: Max, Min and Average of the density and E-Modulus of the right femur model with an acetabular fracture	24
Table 3.5: Max, Min and Average of the density and E-Modulus of the right pelvic model with an acetabular fracture	25
Table 3.6: Max, Min and Average of the density and E-Modulus of the right femur healthy model	26
Table 3.7: Max, Min and Average of the density and E-Modulus of the right pelvic healthy model	27
Table 3.8: Max, Min and Average of the density and E-Modulus of the left femur healthy model	28
Table 3.9: Max, Min and Average of the density and E-Modulus of the left pelvic healthy model	29
Table 3.10 : Magnitude of the applied force	31
Table 4.1: Total deformation, von-Mises and Strain results of the left model with a fracture.	39
Table 4.2: Total deformation, von Mises and Strain results of the right model with a fracture.	39
Table 4.3: Total deformation, von Mises and Strain results of the left model (the healthy subject).	39
Table 4.4: Total deformation, von Mises and Strain results of the right model (the healthy subject).	39
Table 4.5: Total deformation, von-Mises and Strain results of the right model with a fracture (includes articular cartilage).	40



LIST OF FIGURES

	<u>Page</u>
Figure 1.1 : Pelvis and acetabulum connection.....	1
Figure 2.1 : Cortical and trabecular bone [32]......	6
Figure 2.2 : (a) The hip bones articulations, (b) Hip joint.....	7
Figure 2.3 : The Judet and Letournel acetabular fracture classification [41].	8
Figure 2.4 : Elements and Nodes.	10
Figure 2.5 : Force and displacement on the spring.	11
Figure 2.6 : Force - displacement graph.	11
Figure 2.7 : Stress and strain relationship.	12
Figure 3.1 : Flow diagram of the process.....	15
Figure 3.2 : (a) 3D image of a patient with acetabular fracture from CT Scans, (b) 3D image of the healthy subject from CT Scans.....	16
Figure 3.3 : The right side of the patient with a fracture, (a) 3D Model of the cortical femur head, (b) 3D Model of the trabecular femur head.	17
Figure 3.4 : The right side of the patient with a fracture, (a) 3D Model of the cortical pelvic, (b) 3D Model of the trabecular pelvic.....	17
Figure 3.5 : (a) 3D Model of right femur head of the healthy subject, (b) 3D Model of left femur head of the healthy subject.....	18
Figure 3.6 : 3D Model of cartilage.....	18
Figure 3.7 : (a) Pelvis model created using tetrahedron mesh, (b) Femur model created using tetrahedron mesh, (c) Most usual 3D elements.....	19
Figure 3.8 : Distribution of left femur material characteristics of the patient with acetabular fracture.	22
Figure 3.9 : Density and E-Modulus distribution on material numbers.....	22
Figure 3.10 : Distribution of left pelvic material characteristics of the patient with an acetabular fracture.	23
Figure 3.11 : Density and E-Modulus distribution on material numbers.....	23
Figure 3.12 : Distribution of right femur material characteristics of the patient with an acetabular fracture.	24
Figure 3.13 : Density and E-Modulus distribution on material numbers.....	24
Figure 3.14 : Distribution of right pelvic material characteristics of the patient with an acetabular fracture.	25
Figure 3.15 : Density and E-Modulus distribution on material numbers.....	25
Figure 3.16 : Distribution of right femur material characteristics of the healthy subject.	26
Figure 3.17 : Density and E-Modulus distribution on material numbers.....	26
Figure 3.18 : Distribution of right pelvic material characteristics of the healthy subject.	27
Figure 3.19 : Density and E-Modulus distribution on material numbers.....	27

Figure 3.20 : Distribution of left femur material characteristics of the healthy subject.....	28
Figure 3.21 : Density and E-Modulus distribution on material numbers.....	28
Figure 3.22 : Distribution of left pelvic material characteristics of healthy.	29
Figure 3.23 : Density and E-Modulus distribution on material numbers.....	29
Figure 3.24 : Boundary conditions for pelvic (A and B surface is fixed support, C surface is frictionless support).....	30
Figure 3.25 : The force applied to the femur.	31
Figure 3.26 : Cleaning trabecular bone for calculating cortical thickness in a slice.	32
Figure 4.1 : Analysis of the left model of the patient with a fracture, (a) Total deformation, (b) Total deformation for each model, (c) Equivalent (von-Mises) Stress for each model, (d) Equivalent Elastic Strain for each model.....	34
Figure 4.2 : Analysis of the right model of the patient with a fracture, (a) Total deformation, (b) Total deformation for each model, (c) Equivalent (von-Mises) Stress for each model, (d) Equivalent Elastic Strain for each model.....	36
Figure 4.3 : Analysis of the left model of the healthy subject, (a) Total deformation (b) Total deformation for each model, (c) Equivalent (von-Mises) Stress for each model, (d) Equivalent Elastic Strain for each model.....	37
Figure 4.4 : Analysis of the right model of the healthy subject, (a) Total deformation, (b) Total deformation for each model, (c) Equivalent (von-Mises) Stress for each model, (d) Equivalent Elastic Strain for each model.....	38
Figure 4.5 : (a) The right model with a fracture (includes articular cartilage), (b) Femur is hidden to show the distribution of strain, (c) The right model without articular cartilage.....	41
Figure 4.6 : Probable fracture path estimation of the right model with a fracture	41

BIOMECHANICS OF ACETABULAR FRACTURES WITH LOW ENERGY TRAUMA VIA FINITE ELEMENT MODELING AND ANALYSIS

ABSTRACT

The skeletal system undertakes many tasks such as the movement of the body, mineral storage, and protection of soft tissues. Damage to this structure affects human life negatively. Fractures that occur in the human body is damage to mainly to the bone structure and associated surrounding tissues. Therefore, it is necessary to understand how the fractures are formed and the fracture mechanism. Furthermore, the mechanism of fracture is complicated and worthy of investigation. However, the examination of the bone is difficult because it is a structure covered with tissues like veins and muscles. It is not possible to perform mechanical tests of the bones over a living body. On the other hand, these experiments might be carried out on cadavers with permits received. Finding the cadaver and obtaining the necessary permissions is a very demanding task due to ethical regulations.

As a more practical solution, biomechanical models have been alternative due to the advantages in computer technologies. Computer built models are utilized for simulating the effects over biomechanical mechanism *in silico*. The validations and verifications are performed to compare the results with the experimental test results. To perform computational analyzes, first of all, the 3D image of the region of interest is required. With the development of technology, radiological imaging methods have been developed and imaging of the bone without any surgery has been provided. Devices such as Computed Tomography (CT), Magnetic Resonance Imaging (MRI) offer the possibility to view morphology of the human without any operation. These devices provide much useful information as well as disease diagnosis. With the help of the devices, the material properties of the human bone could be determined for a realistic model to mimic the behaviour of the human body in a computer environment.

Osteoporosis is a type of bone disease in which the bones formed as a result of decreased bone mineral density are fragile. In this study, it is aimed to analyze the acetabular fractures, which are more commonly encountered in the elderly with osteoporosis. As a methodology, CT images of two subjects; an elderly and a youngster, were obtained and a 3D model was created utilizing Finite Element Modeling (FEM) technique. In this model, femur, acetabular and as well as articular cartilage were included. Material properties were determined by using the CT values of the created models and transferred to the software for analysis. For material modelling, anisotropic features were extracted. After establishing the contact area and the boundary conditions between the bones, the force was applied to create a sideways fall fracture to the femur trochanter major in the model. Stress-strain values were calculated by using 4-noded tetrahedral meshing in ANSYS. The von Mises values of the left and right models of the healthy subject were 467 MPa and 301 MPa, respectively, and these values were 174 MPa and 142 MPa, respectively, in the patient who had a fracture. According to the results, the von Mises value was 141.59 MPa in the cartilage model and 142.25 MPa without cartilage model in the patient. As the difference is small enough to be neglected, no separate cartilage model is formed for each model.



DÜŞÜK ENERJİ TRAVMALI ACETABULAR KIRIKLARININ SONLU ELEMANLAR MODELİ VE ANALİZİ

ÖZET

İskelet sistemi vücudun hareketi, mineral deposu, yumuşak dokuların korunması gibi pek çok görevini üstlenmiştir. Bu yapının hasar görmesi insan hayatını olumsuz etkilemektedir. İnsan vücudunda meydana gelen kırıklar, temel olarak kemik yapısına ve etrafındaki dokulara zarar verir. Bu nedenle kırıkların nasıl oluştuğunu ve kırık mekanizmasını anlamak gerekir. Ayrıca kırık mekaniği karmaşıktır ve araştırmaya değerlidir. Fakat kemiğin etrafı damar ve kaslar ile örtülü olduğu için incelemek zordur. İnsan hayatta iken kemiklerin mekanik testlerini üzerinde gerçekleştirmek mümkün değildir. Diğer yandan bu deneyler ancak kadavra üzerinde, alınan izinler ile gerçekleştirilebilir. Kadavrayı bulmak ve gerekli etik izinleri almak oldukça zahmetli bir iştir.

Pratik bir çözüm olarak biyomekanik modeller, bilgisayar teknolojilerinin avantajları nedeniyle alternatif olmuşlardır. Bilgisayar modellerinde simülasyonlardan faydalanılmıştır. Validasyon, model sonuçlarını deneysel test sonuçları ile kıyaslanarak yapılır. Analizleri gerçekleştirmek için öncelikle ilgi alanının 3D görüntüsü gereklidir. Teknolojinin gelişmesiyle beraber radyolojik görüntüleme yöntemleri gelişmiş ve kemiğin herhangi bir operasyon olmadan görüntülenmesi sağlanmıştır. CT, MR gibi cihazlar, herhangi bir işlem olmaksızın insanın morfolojisini görüntüleme olanağı sunar. Bu cihazlar hastalık teşhisinin yanı sıra birçok yararlı bilgi sağlar. Günümüz teknolojisinin görüntüleme teknikleri, insan kemiğinin malzeme özellikleri, insan vücudunun bilgisayar ortamındaki davranışını taklit edecek şekilde modelin gerçekliğini artırmak için kullanılabilir.

Osteoporoz, kemik mineral yoğunluğunun azalması sonucu oluşan kemiklerin kırılma eğilimi taşıdığı bir tür kemik hastalığıdır. Bu çalışmada osteoporozlu yaşlılarda daha çok görülen asetabular kemik kırılmasının sonlu elemanlar analizi incelenmesi amaçlanmıştır. Bunun için yaşlı ve genç olmak üzere iki hastanın CT görüntüsü elde edilmiş ve 3 boyutlu modeli sonlu elemanlar modelinden (SEM) faydalanarak çıkarılmıştır. Bu modelde femur, kırık ve asetabular yer almıştır. Oluşturulan modellerin CT değerlerinden faydalanarak malzeme özellikleri belirlenmiş ve sonlu elemanlar analizi için programa aktarılmıştır. Model anizotropik malzeme özellikleri kullanılarak tasarlanmıştır. Kemikler arasında ilişkilerin ve sınır şartlarının belirlenmesinden sonra, femur trochanter majorüne yanal düşme kırılması yaratacak kadar kuvvet uygulanmıştır. Gerilim ve gerinim değerleri ANSYS'de 4-noded tetrahedral mesh kullanılarak hesaplandı. Sağlıklı bireyin sağ ve sol modellerinin von Mises değerleri, sırasıyla 467 MPa ve 301 MPa ve bu değerler kırık taşıyan hastada ise sırasıyla 174 MPa ve 142 MPa olarak bulunmuştur. Kırık taşıyan bireyde elde edilen sonuçlara göre von Mises değeri kırık modelinde 141.59 MPa ve kırık olmayan modelde 142.25 MPa olarak bulunmuştur. Geliştirmiş olduğumuz modelde, fark ihmal edilebilecek kadar küçük olduğundan, her model için ayrı bir kırık model oluşturulmamıştır.



1. INTRODUCTION

Bones are the most vital structures in humans that facilitate motion. The force required for movement is created by the muscle tissues around the bone. These forces help the movement of people, which also supports the body to carry loads. Knowing the locations and number of bones that provide the movement of the human is important to understand the mechanism of motion. The number of bones that a person has is 206 in adults and 270 in a newborn skeleton. In adults, 64 of these bones constitute the upper extremity and 62 constitute the lower extremity [1]. In these bones, the weight of the head, body and the upper extremity is distributed towards the lower extremity under the influence of gravity. Thereby, the lower extremity bones are very strong because they carry the entire weight of the body. One of the most important lower extremity bones is the pelvis. The pelvis is attached to the femur with acetabulum (Figure 1.1). The acetabulum is similar to the pit, which allows movement of the femur head and the hip joint. The cartilage surface that fills between the femur and the acetabulum prevents the two rigid structures from abrading each other and provides very low friction while gliding over each other.

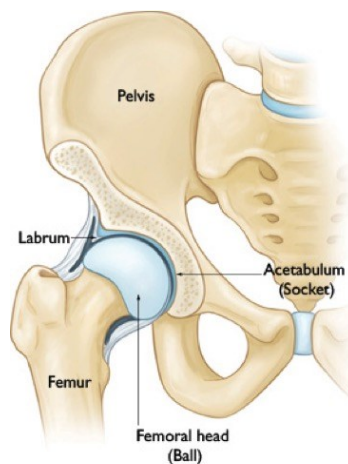


Figure 1.1 : Pelvis and acetabulum connection.

Bone hard tissue provides strength and movement and also stores minerals which are important for the body [2]. Stored minerals form a density in the bone and this is called bone mineral density (BMD). Depending on BMD, the stiffness of the bone changes. In other words, it is a method of measuring bone strength. When BMD decreases, bone resorption, osteoporosis, occurs and the bone becomes weaker and fragile. By inspecting the BMD value, a prediction could be made for foreseeable fractures and diagnosis of osteoporosis [3].

When the bone becomes feeble, there may be fractures in these bones resulting from the falls or various accidents according to the BMD. These fractures are divided into high energy or low energy fractures. For example, falling down while walking and fractures due to high-speed car crash accidents, would fall into low-energy and high energy fractures segments, respectively.

Nowadays, imaging methods have improved substantially, making a diagnosis of the fractures and injuries to the surrounding soft tissues. Computed tomography (CT), an imaging modality, is used for the diagnosis of osteoporosis. Dual-energy X-ray absorptiometry (DXA) works very similar to CT. Depending on CT devices, a 3-dimensional (3D) model can be created by combining the sections, obtained from the scan results covering 360-degree range.

Generated images are generally used in diagnostics and mechanical analysis. One of the mechanical analysis methods is Finite Element Analysis, which performs calculations on the computer. The analysis can be carried out in 2D and 3D. 3D analyses are more preferred in biological structures, for biofidelity reasons. According to the FEA method, after the model is created, it is divided into elements. This process is called meshing. For accurate analysis, the number of elements to be used in the model must have a high mesh ratio. But the increasing the number of elements increases the time required to calculate the results. Therefore many researchers have simplified the model to solve this problem using an optimum number of elements [4]. Another important issue is to determine the material properties used in the model. The material can be chosen to be heterogeneous or homogeneous. In some studies, there has not been much difference between these two materials, with little impact over the

results [5]. But, in most studies, it was said that heterogeneous material properties provide better results [6].

Finite Element Modeling (FEM) facilitates the biomechanical analysis of tissues. It has been pointed out in many studies that the conditions show close enough results to reality when modelled correctly [7-8]. In FEM, many analyses could be performed that could not be possible to perform without damaging the model in vivo.

There are two types of FEA orthopaedic biomechanics, muscle skeleton study and mechanical structure study. Muscle activity and kinematics of the skeletal system are examined in musculoskeletal studies, while the stress-strain analyses of bone or implants are investigated in mechanical structure studies [9]. The second group of studies is frequently used in the field of orthopaedic biomechanics.

Fractures can be classified in terms of energy density. High energy fractures occur as a result of motor accidents or trauma, while low energy fractures are caused by falls as they walk or stand [10].

In this study, patient-specific CT-based finite element analysis was performed. It is aimed to understand and analyse low-energy acetabulum fractures. CT images of a patient with an acetabular fracture and that of a healthy person who does not have this condition were taken and 3-dimensional models were extracted. The region of interest to be examined is obtained from the CT images. The CT images are smoothed and transferred to the FE software. Then the material characteristics and the boundary conditions acting on the tissue were determined.



2. LITERATURE REVIEW

Many studies have been made previously to examine the bone biomechanics [11-12]. These studies utilised computer-assisted simulation methods. However, analysis on the computer alone is not sufficient to understand the biomechanical properties of bone. To validate the models, mechanical tests are required as well. Thus, mechanical tests were performed and both experimental and computational analysis studies were compared [13]. By comparing the computer simulations and the experimental work, validation is completed. However, this requires a cadaveric bone for CT scanning and mechanical testing. Mechanical characterization of bone is achieved by using the cadaveric bones using mechanical testing instruments. But finding the cadavers and getting the necessary permits is very troublesome. Additionally, it is difficult to mount the specimen with the correct orientation to the mechanical test device. On the other hand, many studies have shown that there are not many differences between the experimental data and the computational biomechanics [14]. From this point of view, correct modeling and analysis have been shown to lead to the right path. In some studies, not only the bony structure was considered but also muscle and cartilage were added to the analysis [15-16]. However, such modeling takes a lot of time and it is quite complicated [17]. As the model to be analysed approaches realistic conditions, it becomes increasingly difficult to model this complex phenomenon in a computer environment. Furthermore, the bone is not a homogeneous material. However, the bone could be considered as homogeneous or heterogeneous material in FEM. In the homogeneous structure, single material property is assigned to the bone, while in the heterogeneous structure, the bone is divided into two structures as a trabecular and a cortical bone as detailed below. In some studies, the bone is divided into trabecular and cortical bone and in some cases, it is regarded as a single bone because there is not much difference between them in terms of material properties [18].

2.1 Bone - A brief anatomical review

Bone is a structure which continuously renews itself. This process continues through the various bone cells it contains. However, the cells in the bones are continuously generated and destroyed. As this process ages, it reverses its direction and destruction begins to increase [19-20-21]. Bone cells are classified into 4 types including osteoblasts, bone lining cells, osteocytes, and osteoclasts [22-23]. Osteoblasts are those cells located along the bone surface and involved in bone formation [24]. Osteoclasts are multi-nucleated large bone cells involved in bone destruction and involved in the mononuclear phagocyte system [25]. Osteocytes are cells in the lacunae, responsible for the preservation of the long-lived bone matrix and 90-95% of total bone cells [26-27]. Bone lining cells are the cells that sit on the outside of the bone and surround the bone surface, shortly regulating mineral homeostasis [28].

Skeleton performs several tasks. These include movement, support, protection of soft tissues, mineral storage and bone marrow harbouring [29-30]. Bone tissue can be seen in two forms, cortical and trabecular. Cortical bone is also called compact bone. Cortical bone forms the cortex, or outer shell, of most bones. It is much denser than trabecular bone. Trabecular bone makes up the inner layer of the bone and it is also known as cancellous or spongy bone tissue [31]. Trabecular bone has a higher surface area but is less dense, softer, weaker, and less stiff. It typically occurs at the ends of long bones, proximal to joints and within the interior of vertebrae. Cortical and trabecular bones are shown in Figure 2.1.

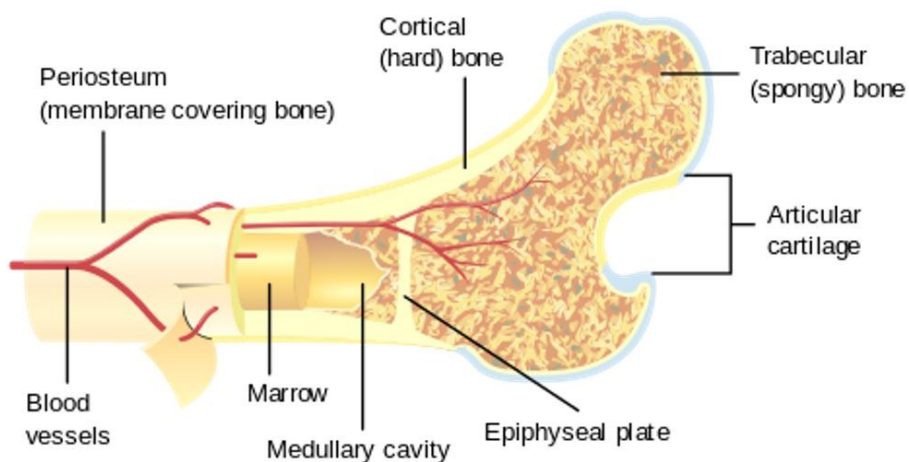


Figure 2.1 : Cortical and trabecular bone [32].

Nowadays, osteoporosis is defined as a systemic disease that is characterized by low bone density and deterioration of bone structure and increases in the tendency of bone to break making it fragile. This disease can occur if the destruction of bone cell rate is higher than the rate of construction. Bones become more brittle due to bone resorption and may fracture with a small effect. The probability of osteoporosis increases depending on age [33].

When the anatomical structure of hip bones are examined, the left and right hip bones (innominate bones, pelvic bones) are two irregularly shaped bones that form part of the pelvic bone. The hip bones have three main articulations such as sacroiliac joint, pubic symphysis and hip joint (Figure 2.2(a)). The sacroiliac joint is the formation between the auricular surfaces of the sacrum and ilium. Pubic symphysis formed by the articulation between the pubic bodies of the right and left hip bones. The hip joint is formed by the union of the acetabulum and femur head (Figure 2.2(b)). The bones of the pelvis are strongly joined together to form a substantially immobile, weight-bearing structure. This is important for stability because it allows the body's weight to be easily transferred from the vertebral column, through the pelvic girdle and hip joints. The hip bone is brought about by three separate bones that fuse together during the late teenage years. These bony parts are the ilium, ischium, and pubis. Hip bones are inspected under two categories as right and left [34].

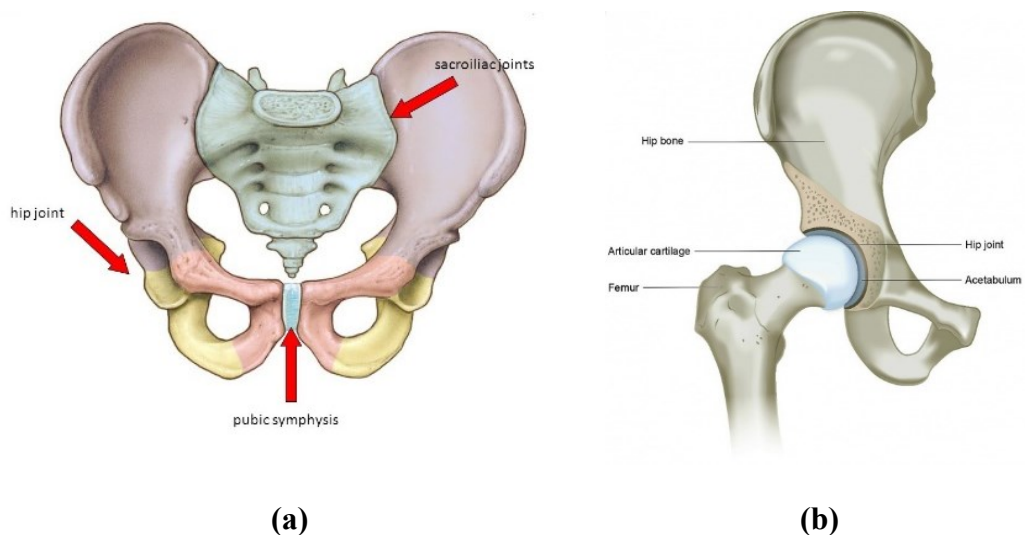


Figure 2.2 : (a) The hip bones articulations, (b) Hip joint.

2.2 Acetabular fracture types

Acetabulum fractures can involve one or more of the two columns, two walls or roof within the pelvis [35]. They occur much less frequently than fractures of the upper femur or femoral head [36]. Treatment for acetabular fractures often involves surgery to restore the normal anatomy of the hip and stabilize the hip joint. These fractures appear in two forms [37].

- High energy trauma (e.g., motor vehicle accidents)
- Low energy trauma, more common in the elderly (e.g., fall from standing height)

High energy trauma is a type of trauma that causes serious injuries for any reason. These include falling from three times its own length, motor accidents greater than at 65 km/h, explosions, major burns, and gunshot wounds [38]. Low-energy traumas consist of stabbing, fracture, fall from standing, and low-velocity injuries [39]. Both types of trauma may result in a fatal. While 41% of the deaths are composed of low-energy trauma, 59% consist of high-energy trauma [40].

Acetabular fractures vary (Figure 2.3). For example, the bone can break straight across the socket or shatter into many pieces. When the acetabulum is fractured, the femoral head may no longer fit firmly into the socket, and the cartilage surface of both bones could be damaged. If the joint remains irregular or unstable, ongoing cartilage damage to the surfaces could lead to arthritis [37].

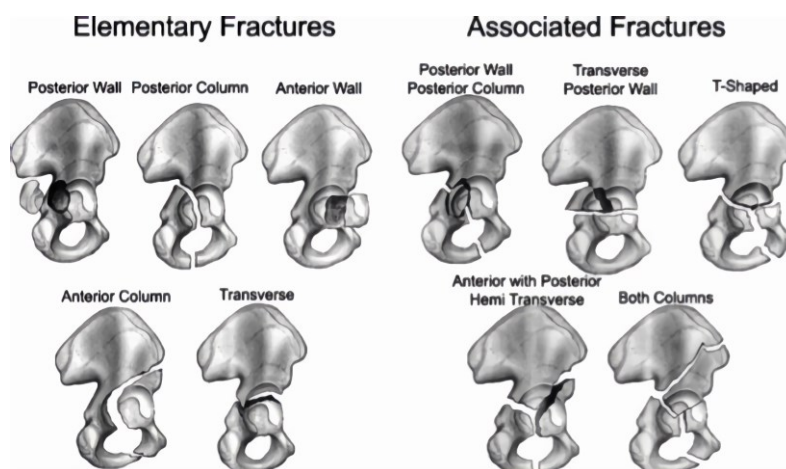


Figure 2.3 : The Judet and Letournel acetabular fracture classification [41].

2.3 Imaging Methods

Radiological imaging is an indispensable point in the diagnosis of the disease. There are many devices and methods used for this purpose. In terms of diagnosis, common imaging types include computed tomography (CT), MRI (Magnetic Resonance Imaging), Ultrasound, and X-ray. These imaging modalities have advantages or disadvantages compared to each other. In X-ray and CT methods, the patient is exposed to harmful X-rays, while MRI and ultrasound imaging have no proven damage to the living organism until now. Nowadays, MRI is used especially for imaging of soft tissues. One of the most important reasons for preferring CT to normal radiological imaging is that higher contrast can be obtained, and another reason can be the capability of CT in taking images from multiple sections, which can provide more details of the imaged tissue. Unlike MRI, CT is usually used for bone injuries and hard tissue imaging. The difference of X-ray imaging from CT imaging is that the patient is less exposed to harmful radiation. As for ultrasound, there is no X-ray in this examination method. Ultrasound is used as an effective imaging method for the examination of organs in which the sound waves like the abdominal organs can easily pass. In this study, CT images were obtained because of hard tissue analysis [42].

2.4 Finite Element Method

FEA is a numerical method designed to solve engineers' problems. It was first used for stress analysis of aircraft bodies in 1956. Later, this method was developed rapidly and applied in other areas [43].

Some of these areas are;

- Mechanical/Aerospace/Civil/Automotive
- Structural Analysis
- Fluid Flow
- Heat Transfer
- Electromagnetic Fields
- Soil Mechanics
- Acoustics
- Biomechanics

With this method, complex geometric shapes are divided into smaller pieces to define a limited number of elements. This process is called meshing. Elements come together to form a node. It simplifies the solution of a limited number of elements connected by nodes [44]. Figure 2.4 shows the elements and the nodes. Then, the structure of the equations is created. The system of equations is solved according to the boundary conditions and the applied load. The result obtained is an approximate solution to the problem. By increasing the number of elements in the model, the result is might get closer to the truth, but then, this is a costly operation in terms of computation time. [45]. For example, as the number of elements increases, the size of the matrix that the computer solves increases so the calculation time increases. FEA can be performed in different dimensions, such as one-dimensional, two- dimensional and three-dimensional. Local elastic behaviour of each element is defined as stiffness, loading, and displacement in matrix form [46].

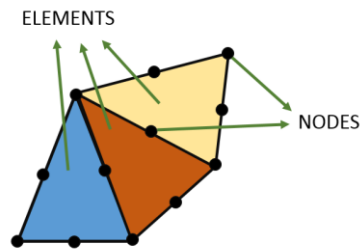


Figure 2.4 : Elements and Nodes.

The simplest spring mechanism has been shown to understand FEA. As shown in Figure 2.5, when the forces f_1 and f_2 are applied, the displacements u_1 and u_2 occur. K is spring stiffness constant. From this, the formula (2.1) is obtained [47].

$$\begin{bmatrix} k & -k \\ -k & k \end{bmatrix} \begin{Bmatrix} u_1 \\ u_2 \end{Bmatrix} = \begin{Bmatrix} f_1 \\ f_2 \end{Bmatrix} \quad (2.1)$$

$$[k_e] \{u\} = \{f\} \quad (2.2)$$

$$k_e = \begin{bmatrix} k & -k \\ -k & k \end{bmatrix} \quad (2.3)$$

where k_e is the stiffness matrix for a spring element, u is the nodal displacement, and f is the nodal force. This matrix contains the geometric and material behaviour of the element. Also, it shows the resistance of the element according to the applied force. Boundary conditions and power are applied to u . In Figure 2.6, the slope gives the stiffness matrix [48].

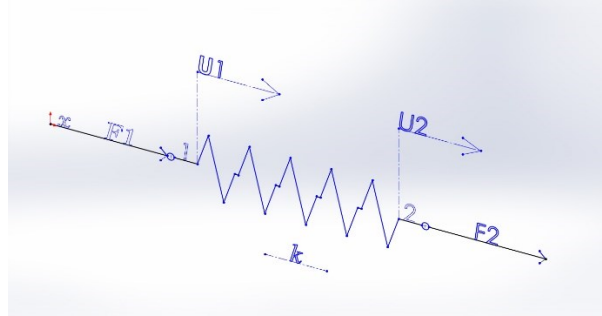


Figure 2.5 : Force and displacement on the spring.

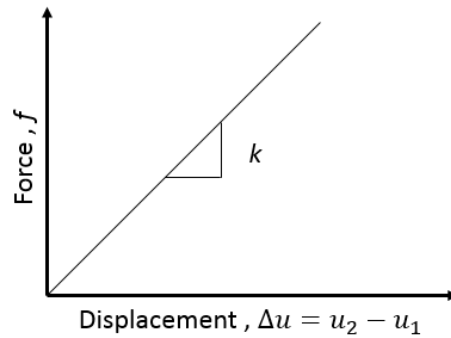


Figure 2.6 : Force - displacement graph.

Since the load and spring constant are known in formula 2.2, displacement can be found. Stress and strain values can be found after u . The strain is the shape or volume variation of the object when the load is applied. The stress is the force per unit area [49].

$$\varepsilon = \frac{\Delta u}{u_0} \quad (2.4)$$

$$\sigma = \frac{F}{A} \quad (2.5)$$

where σ is stress ($\frac{N}{m^2}$), F is a force applied (N), A is an area on which force is acting, and ϵ is strain (no dimension). This value is found by dividing the first length of the total displacement. There are two types of material changes under applied load [50]. If the object returns to its original state after the application of the load, the elastic shape change will occur if it is not plastic. There is a relationship between stress and strain in elastic materials (Figure 2.7). In the 17th century Hooke described this relationship in formula 6 [51].

$$\sigma = E\epsilon \quad (2.6)$$

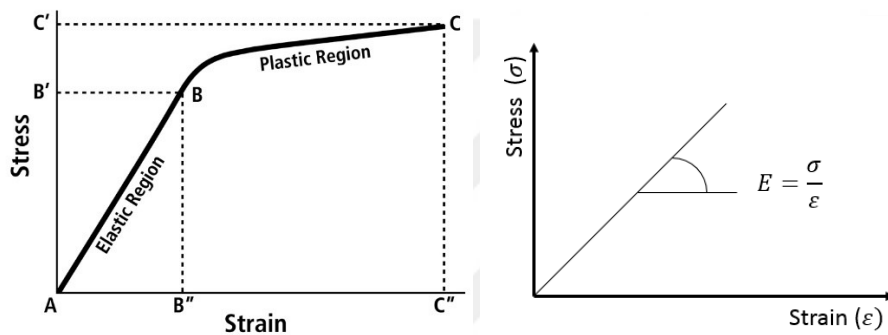


Figure 2.7 : Stress and strain relationship.

Hooke found a linear relationship between stress and strain in the elastic region. The relationship between these two is very similar to the spring model. The slope here gives the value of E instead of k . E is Young's modulus. It is the resistance of the material against flexion and is a material-specific value. For example, this value is 0.01-0.1 GPa for rubber with a large stretch and 200 GPa for less stretch steel. When we come to the bone, since the bone is not homogeneous, this ratio varies between 100MPa and 33 GPa. As the material passes from the elastic region to the plastic region, residual deformation on the material occurs. This transition point is specific and is defined as the yield point. There are several ways to determine this point. After passing a certain force, the material is broken, which is defined as von Mises yield point criterion. The von Mises criterion states that failure occurs when the energy of distortion reaches the same energy for yield/failure in uniaxial tension [52]. Mathematically, this is expressed as,

$$\sigma_v^2 \geq \frac{1}{2} [(\sigma_1 - \sigma_2)^2 + (\sigma_1 - \sigma_3)^2 + (\sigma_2 - \sigma_3)^2] \quad (2.7)$$

where $\sigma_1, \sigma_2, \sigma_3$ are principal stresses. That is, if the von Mises stress is greater than the simple tension yield limit stress, then the material is expected to be broken. The von Mises stress is not true stress. It is a theoretical value that allows the comparison between the general 3D stresses with the uniaxial stress yield limit.

$$\nu = \frac{\varepsilon_y}{\varepsilon_x} \quad (2.8)$$

Poisson Ratio (ν) is a constant obtained by the ratio of the lateral (ε_y) and axial (ε_x) elastic unit deformation of a material in the elastic region (2.8). The poisson ratio of materials is accepted from 0 to 0.5. This number varies for solid materials. For example, the Poisson's ratio for steel is about 0.3, while it is between 0.2 and 0.3 for bone.



3. MATERIALS AND METHODS

3.1 Subjects

CT images of 2 subjects were used for this study. One of them had an acetabular fracture (the patient) while the other one didn't have a fracture or any signs of impairment in the hip joint (healthy subject). CT imaging was performed with a 64-row MD-CT scanner (Sensation 64 and Scope; Siemens Medical Solutions, Erlangen, Germany). One CT image of the patients belonged to an 88-year-old female, while the other CT image was of a 24-year-old healthy male. CT images were obtained after the anonymization process at University of Oulu with the permission of the ethics committee. Since the CT images were anonymized, the previous medical history of the patients and their weight were unknown. In this chapter, we are going to explain the process flow as shown in the flowchart (Figure 3.1).

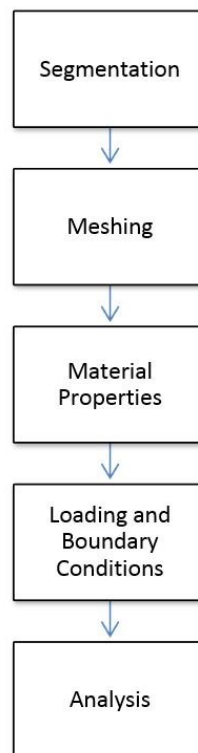


Figure 3.1 : Flow diagram of the process.

3.2 Image Segmentation

Many algorithms were utilised in the segmentation process such as; thresholding, region growing, classifiers, clustering, and artificial neural network. Thresholding algorithm is very simple and useful. The segmentation process was carried out in the MIMICS v17 software (Materialize, Leuven, Belgium), with a licensed program from the University of Oulu. The CT images are processed separately for each bone. The CT data set of the patient with fracture was acquired with the following technological parameters: voltage = 120 kV, slice thickness = 1 mm. The CT grey values of the bone were in terms of Hounsfield units (HU) ranged from -1023 to 1791 HU. The CT-scan images of the pelvic bone of a patient were stored from Siemens Sensation 64 in 512 x 512 pixels, having a pixel size of 0.6426 mm (Figure 3.2(a)). The CT data set of the healthy subject was acquired from Siemens Scope CT with the following technological parameters: voltage = 130 kV, slice thickness = 3mm, matrix (pixel) size 512 x 846, pixel spacing = 0.5. The CT grey value ranged from -1023 to 1550 HU (Figure 3.2(b)).

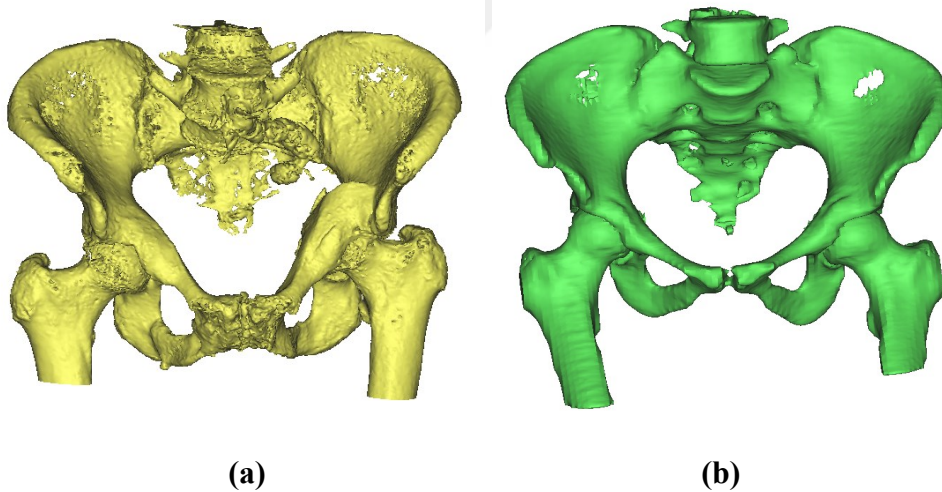


Figure 3.2 : (a) 3D image of a patient with acetabular fracture from CT Scans, (b) 3D image of the healthy subject from CT Scans.

Threshold algorithm was used to separate the skeleton of the healthy subject from the soft tissue and the threshold value was determined as 80 HU (Figures 3.3, and 3.4). The threshold value of the patient with fracture was set at 226 HU (Figure 3.5). The selection of these values was performed manually and tried to give the best results so as to distinguish hard tissue from soft tissue. Sacrum, pelvis and femur bones were

reconstructed based on the calculated values using 3D mask separately. The pelvic and femoral heads were taken into consideration for the right and left parts. The parts obtained separately in 3D were transferred to the 3-MATIC v9 software (Materialize, Leuven, Belgium) for correction. Wrap and smooth processes were performed to eliminate errors, fill gaps and flatten the surface. For the wrap process, the gap closing distance is 0.2 mm and the smallest detail was 1 mm. The smooth factor was 0.7 and the number of iterations was five (Figures 3.3, 3.4, and 3.5). These values were determined manually to give the best results.

Generation of the femur and pelvic:

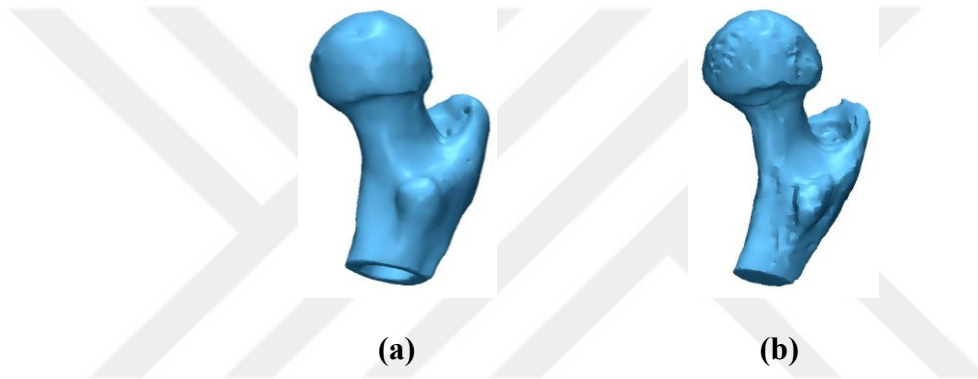


Figure 3.3 : The right side of the patient with a fracture, **(a)** 3D Model of the cortical femur head, **(b)** 3D Model of the trabecular femur head.

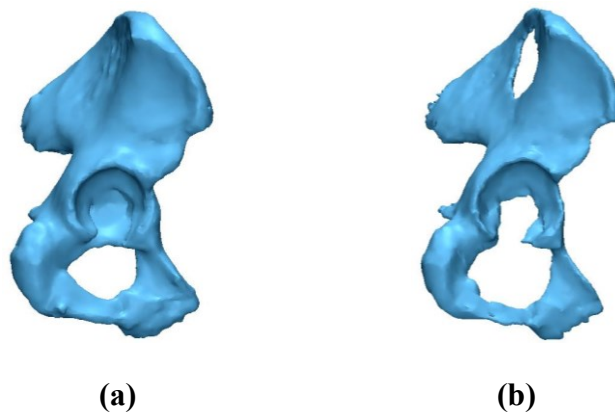


Figure 3.4 : The right side of the patient with a fracture, **(a)** 3D Model of the cortical pelvic, **(b)** 3D Model of the trabecular pelvic.

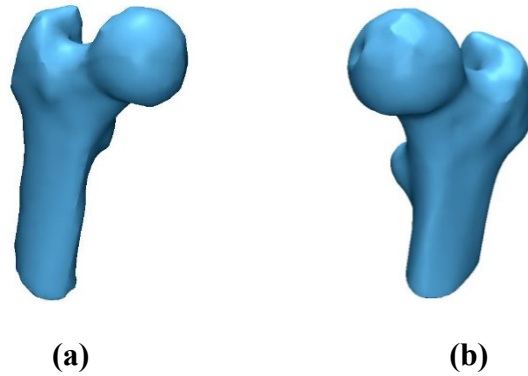


Figure 3.5 : (a) 3D Model of right femur head of the healthy subject, (b) 3D Model of left femur head of the healthy subject.

CT images were converted into the 3D model for each individual part forming the bone joint assembly using the MIMICS v17 (Materialize, Leuven, Belgium). The threshold values of 80 to 1791 HU were used. After the parts were separated from each other, a smooth 3D model was obtained by using the region growing algorithm. The proximal femur and pelvis were separately created, cortical and trabecular models of each bone structure were completed manually (Figures 3.3, and 3.4). Received CT scan showed a fracture in the left acetabulum of the patient. There was no fracture in the right acetabulum. Geometrically damaged areas were corrected by wrapping and smoothing operations.

Generation of the cartilage layer:

Additionally, cartilage was formed from the image. It is difficult for the CT device to display soft tissues. It is better to display soft tissues with MRI systems instead of CT. However, since the patient does not have an MR image, the cartilage can be calculated in 3D using the CT image. So the area between the femur and acetabulum was an approximated modelled by selecting the cartilage in each CT slice (Figure 3.6).

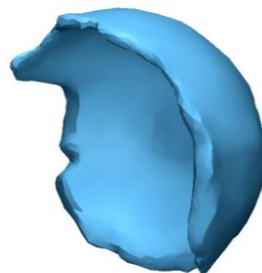
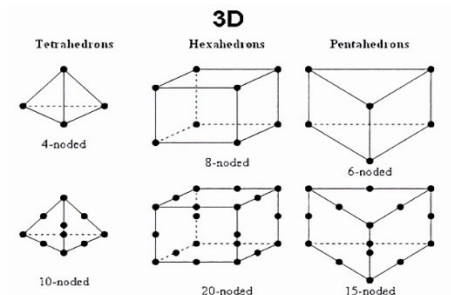
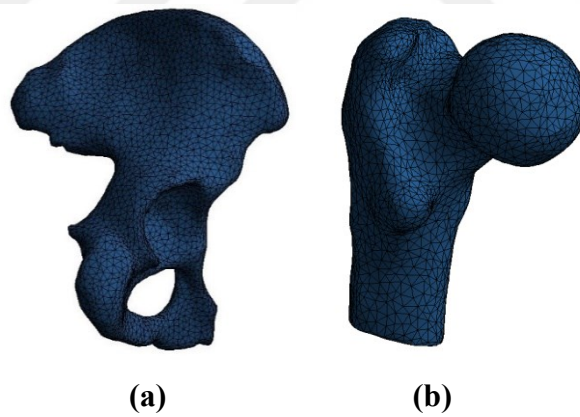


Figure 3.6 : 3D Model of cartilage.

3.3 Meshing

With mesh processing, the rigid body model is divided into the elements. Meshing process is a very important step because it affects the results [53]. Accurate results can be reached only by making proper meshing process. For 3D geometries, there are many forms of meshing that are used in the literature [54-55]. These are shown in Figure 3.7(c). Most of the studies used 4 noded mesh type. If the FE-model is complex and has curved geometries or acute angles, the 4-node mesh method should be selected. However, it takes longer to solve the analysis by tetrahedral mesh method. In this study, the tetrahedron is used because the geometries are complex. Models created using tetrahedron mesh are given in Figure 3.7(a)(b).

There are two ways to produce mesh. These are Voxel-based and commercially available methods. The voxel-based mesh is mentioned [56] to be superior compared to the others. In this study, voxel-based meshing was performed using 3-MATIC. Four-noded linear tetrahedron meshes were created. The number of elements and the number of nodes in the generated mesh are given in Table 3.1.



(c)

Figure 3.7 : (a) Pelvis model created using tetrahedron mesh, (b) Femur model created using tetrahedron mesh, (c) Most usual 3D elements.

Table 3.1 : The number of nodes and the number of elements for each model.

MODEL	#NODES	#ELEMENTS
<i>Subject with acetabular fracture</i>		
Right Femur	16588	9659
Right Pelvic	13332	7237
Total	29920	16896
Left Femur	18985	10993
Left Pelvic	23880	13614
Total	42865	24607
<i>Healthy Subject</i>		
Right Femur	22747	13553
Right Pelvic	21843	12230
Total	44590	25783
Left Femur	14328	8292
Left Pelvic	16643	9106
Total	30971	17398

The geometries were transferred to the ANSYS 16.1 (Workbench, PA, USA) software after finishing the meshing process. At this point, it is necessary to transfer the geometries to the ANSYS in STEP or IGES file format. After transferring one of the geometries, the other geometry is imported as well as in contact with each other. Since two geometries are transferred together with their coordinate systems, no rotate or translate operation is required on ANSYS.

3.4 Material Properties

HU values of CT were used to determine material properties. There is a linear relationship between HU value and apparent density. This relationship has been determined in previous studies [57].

$$\rho_{app} = 1.028 + 0.00769xHU \quad (3.1)$$

where ρ_{app} is apparent density and HU (Hounsfield Units) is CT value. Materials are classified as isotropic, anisotropic and orthotropic according to their construction. The isotropic material mechanically shows the same property in every direction, while the

anisotropic materials mean not having uniform mechanical and thermal properties in every direction [58]. The materials whose properties vary in three perpendicular directions are called orthotropic materials. Although the bone has orthotropic properties, modeling it with this assumption is challenging [59]. In addition, it is very challenging to calculate and transfer the elastic modulus of the orthotropic material. In previous studies, it was found that there was not much difference between orthotropic and anisotropic [60]. Model-based on anisotropic material properties have more accurate results than isotropic materials [61 -62]. In this study, the bone was treated as anisotropic. Bone structure is heterogeneous in itself. Material properties may vary from region to region. The elastic modulus of the bone can also vary within the voxel. Taking advantage of CT values, each voxel in Young's modulus was found using formula 8-9.

$$\varepsilon = 0.06 + 0.09\rho_{app}^{7.4} \quad (3.2)$$

The Poisson's ratio was determined as 0.3 according to the model by using the previous researches [63-64]. Material properties were determined separately for each element. At this point, the number of materials was chosen to be 100. So ranging from 1 to 100 different material properties were created for each bony part of the model components. The Young's modulus and Poisson ratios of these materials were calculated using equation 3.1 and 3.2.

Material properties of each voxel were determined by MATLAB (R20015b, MathWorks, Inc., Natick, MA, USA). The material map has been extracted using the HU value for each pixel of the CT image. Trabecular and cortical bone material properties were determined separately for the femur and pelvic bones. Distribution of material properties is shown in Figures 3.8, 3.10, 3.12, 3.14, 3.16, 3.18, 3.20, and 3.22. The density and the E-Modulus values of all models are given in Tables (Tables 3.2, 3.3, 3.4, 3.5, 3.6, 3.7, 3.8, and 3.9). The distribution of 100 different material properties is shown in Figures for each model (Figures 3.9, 3.11, 3.13, 3.15, 3.17, 3.19, 3.21, and 3.23). After the material properties have been determined, they were transferred to the ANSYS for analysis. The code used for this is provided in the appendix.

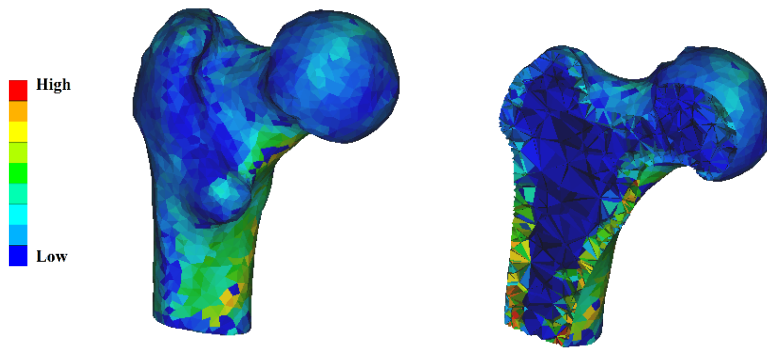


Figure 3.8 : Distribution of left femur material characteristics of the patient with acetabular fracture.

Table 3.2: Max, Min and Average of the density and E-Modulus of the left femur model with an acetabular fracture

	<i>Density (g/cm³)</i>	<i>E-Modulus (GPa)</i>
<i>Max</i>	2,023	16,592
<i>Median</i>	1,481	3,776
<i>Min</i>	0,939	0,117

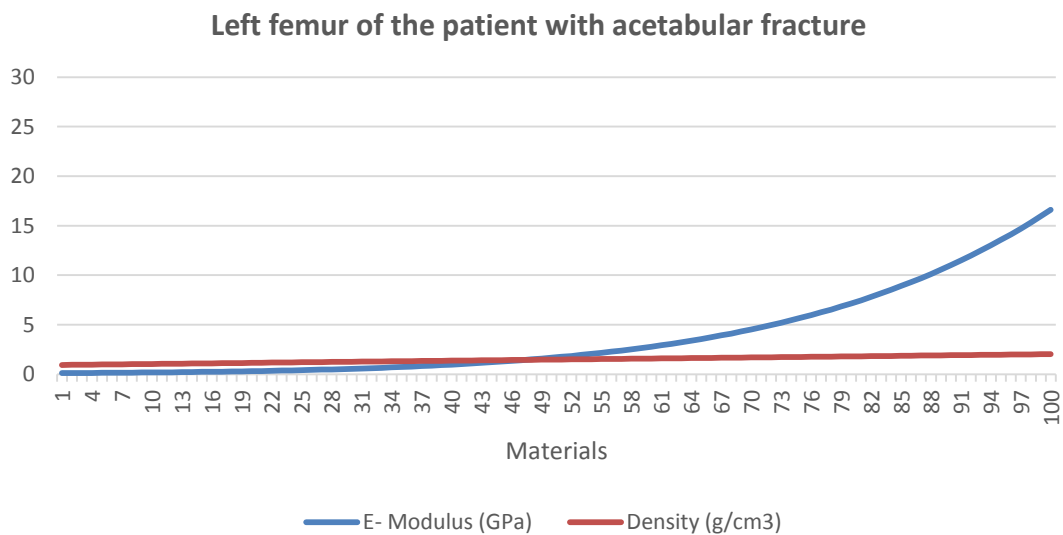


Figure 3.9 : Density and E-Modulus distribution on material numbers.

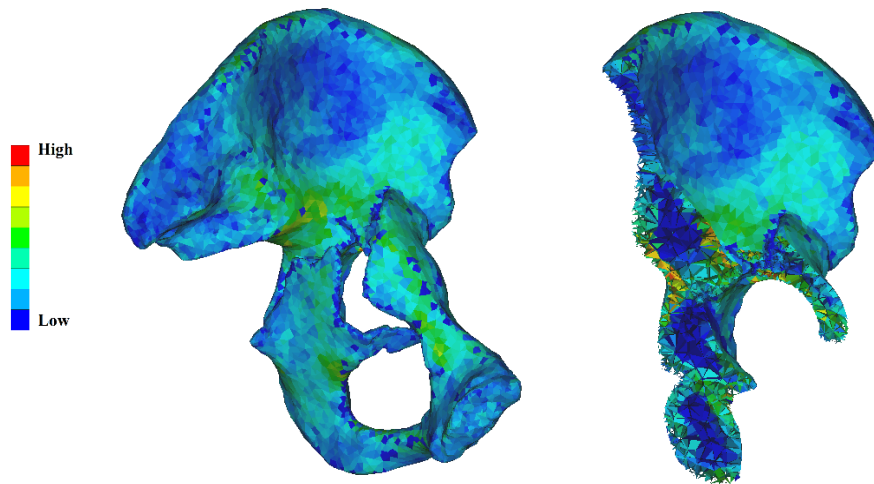


Figure 3.10 : Distribution of left pelvic material characteristics of the patient with an acetabular fracture.

Table 3.3: Max, Min and Average of the density and E-Modulus of the left pelvic model with an acetabular fracture

	Density (g/cm^3)	E-Modulus (GPa)
Max	1,736	5,403
Median	1,342	1,468
Min	0,949	0,121

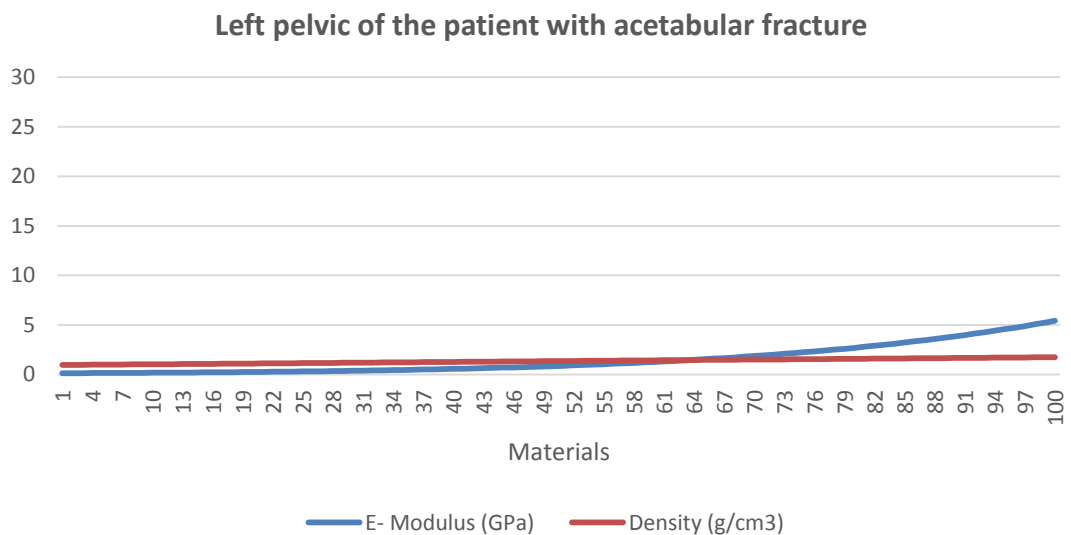


Figure 3.11 : Density and E-Modulus distribution on material numbers.

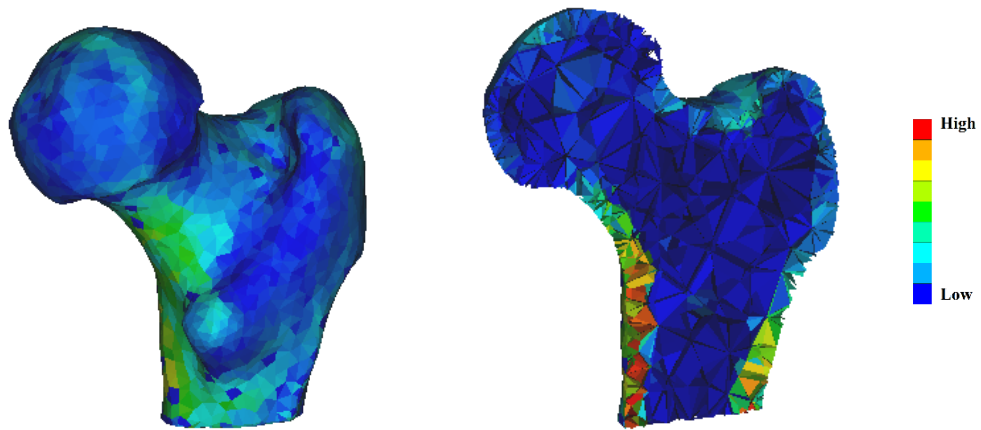


Figure 3.12 : Distribution of right femur material characteristics of the patient with an acetabular fracture.

Table 3.4: Max, Min and Average of the density and E-Modulus of the right femur model with an acetabular fracture

	<i>Density (g/cm³)</i>	<i>E-Modulus (GPa)</i>
<i>Max</i>	2,084	20,687
<i>Median</i>	1,512	4,584
<i>Min</i>	0,939	0,117

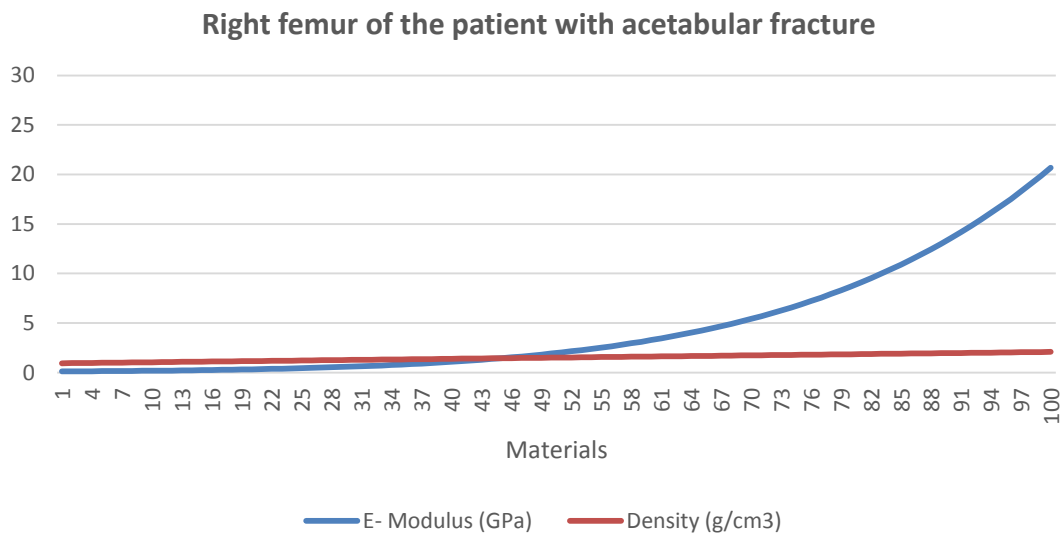


Figure 3.13 : Density and E-Modulus distribution on material numbers.

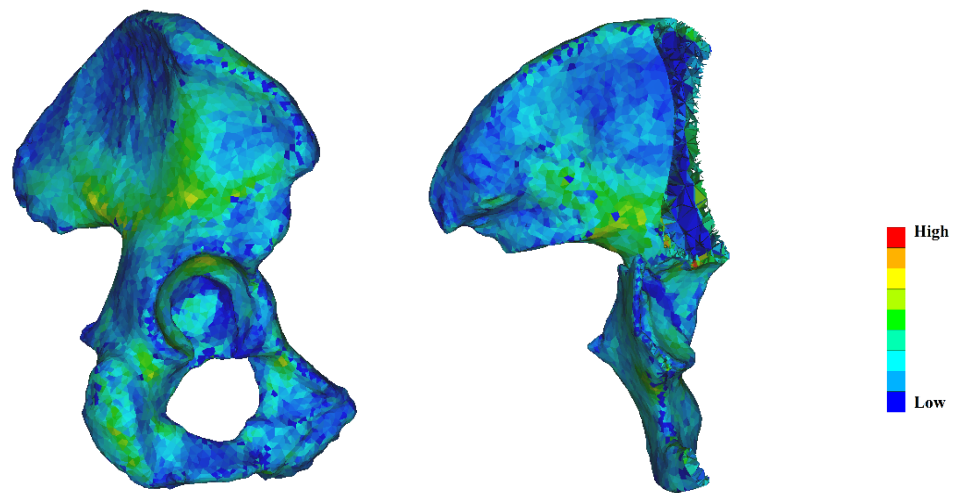


Figure 3.14 : Distribution of right pelvic material characteristics of the patient with an acetabular fracture.

Table 3.5: Max, Min and Average of the density and E-Modulus of the right pelvic model with an acetabular fracture

	<i>Density (g/cm³)</i>	<i>E-Modulus (GPa)</i>
<i>Max</i>	2,093	21,317
<i>Median</i>	1,516	4,710
<i>Min</i>	0,940	0,117

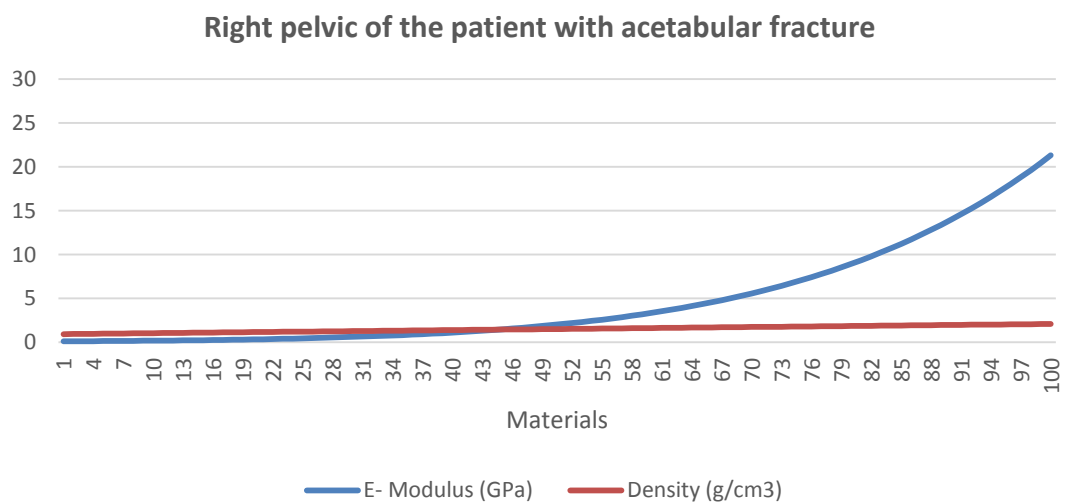


Figure 3.15 : Density and E-Modulus distribution on material numbers.

Material characteristics of femoral and pelvic bones were determined using the same formula as before.

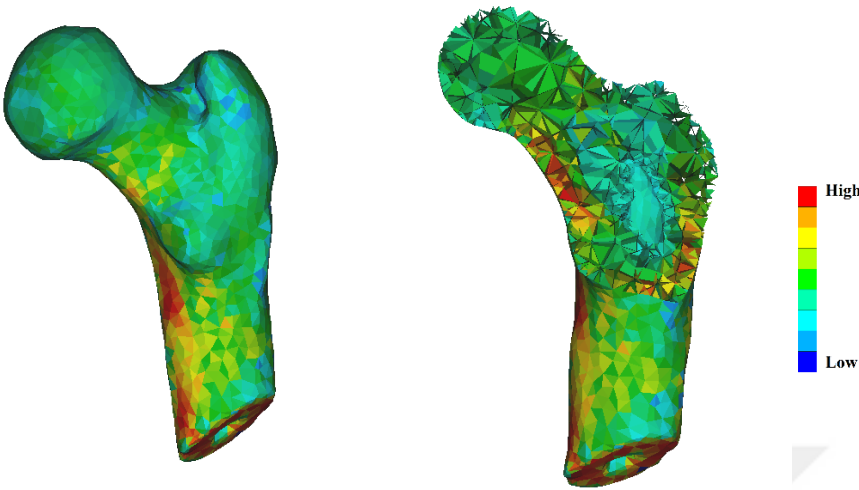


Figure 3.16 : Distribution of right femur material characteristics of the healthy subject.

Table 3.6: Max, Min and Average of the density and E-Modulus of the right femur healthy model

	Density (g/cm ³)	E-Modulus (GPa)
Max	2,143	25,392
Median	1,455	4,834
Min	0,766	0,073

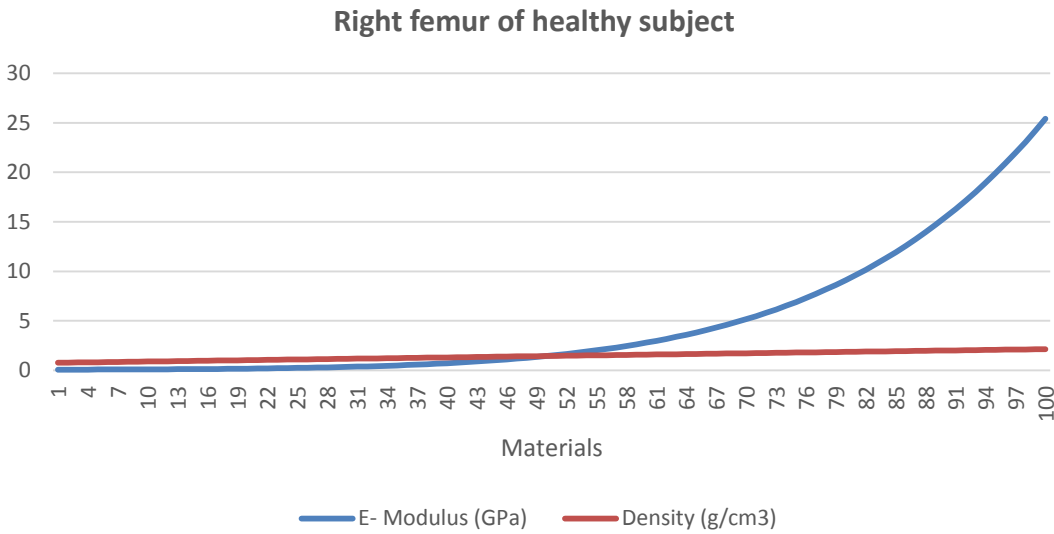


Figure 3.17 : Density and E-Modulus distribution on material numbers.

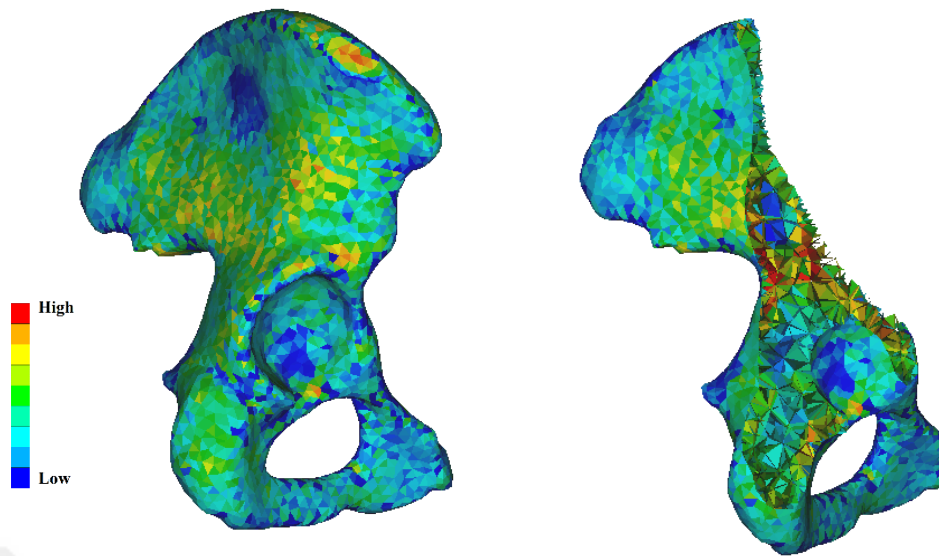


Figure 3.18 : Distribution of right pelvic material characteristics of the healthy subject.

Table 3.7: Max, Min and Average of the density and E-Modulus of the right pelvic healthy model

	<i>Density (g/cm³)</i>	<i>E-Modulus (GPa)</i>
<i>Max</i>	1,838	8,206
<i>Median</i>	1,436	2,276
<i>Min</i>	1,033	0,174

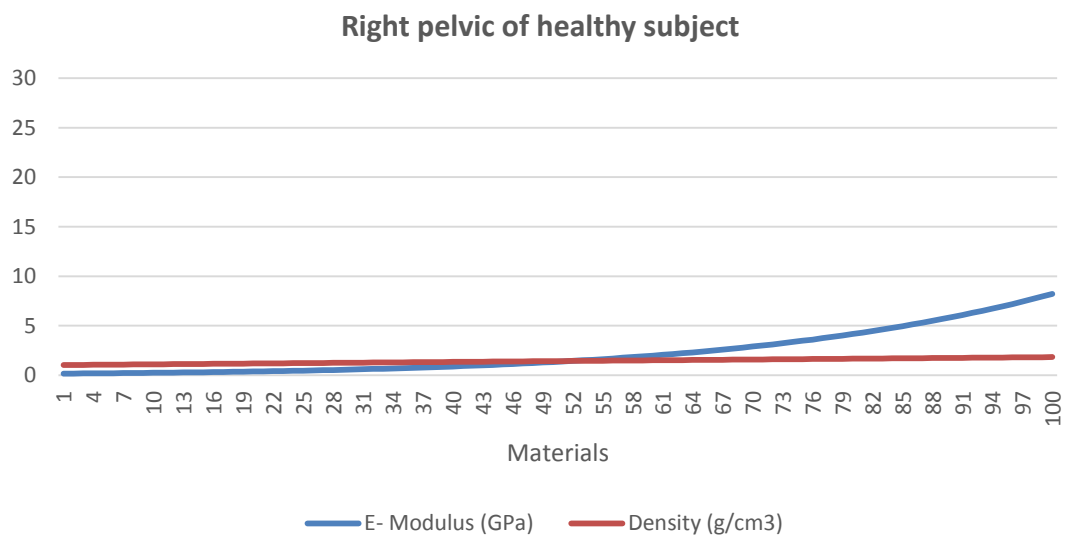


Figure 3.19 : Density and E-Modulus distribution on material numbers.

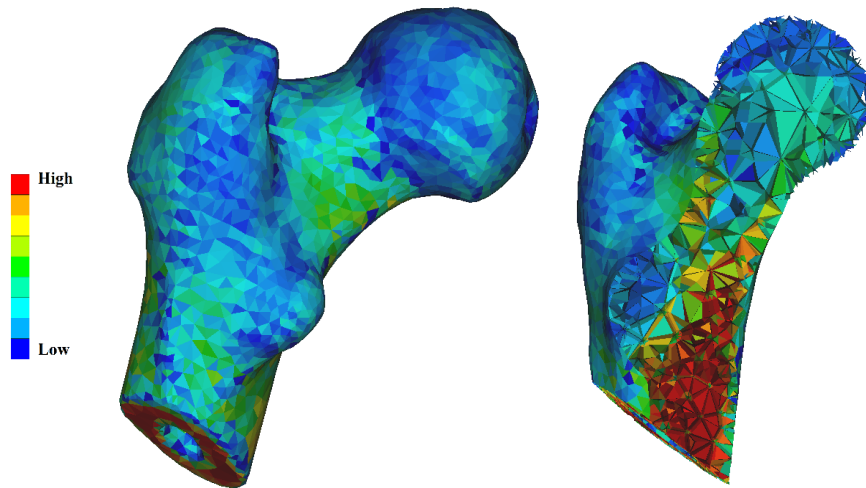


Figure 3.20 : Distribution of left femur material characteristics of the healthy subject.

Table 3.8: Max, Min and Average of the density and E-Modulus of the left femur healthy model

	<i>Density (g/cm³)</i>	<i>E-Modulus (GPa)</i>
<i>Max</i>	2,174	28,258
<i>Median</i>	1,598	6,467
<i>Min</i>	1,022	0,166

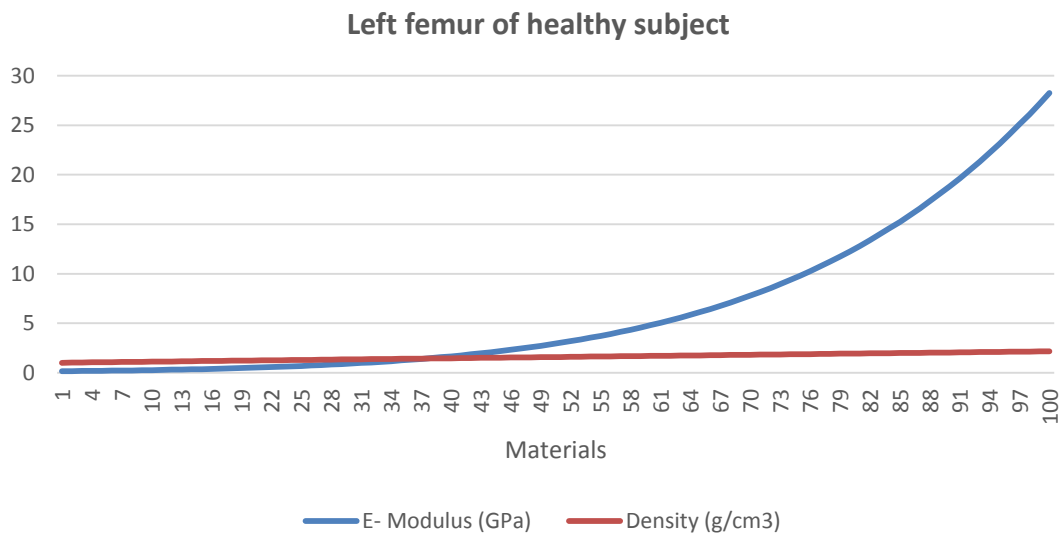


Figure 3.21 : Density and E-Modulus distribution on material numbers.

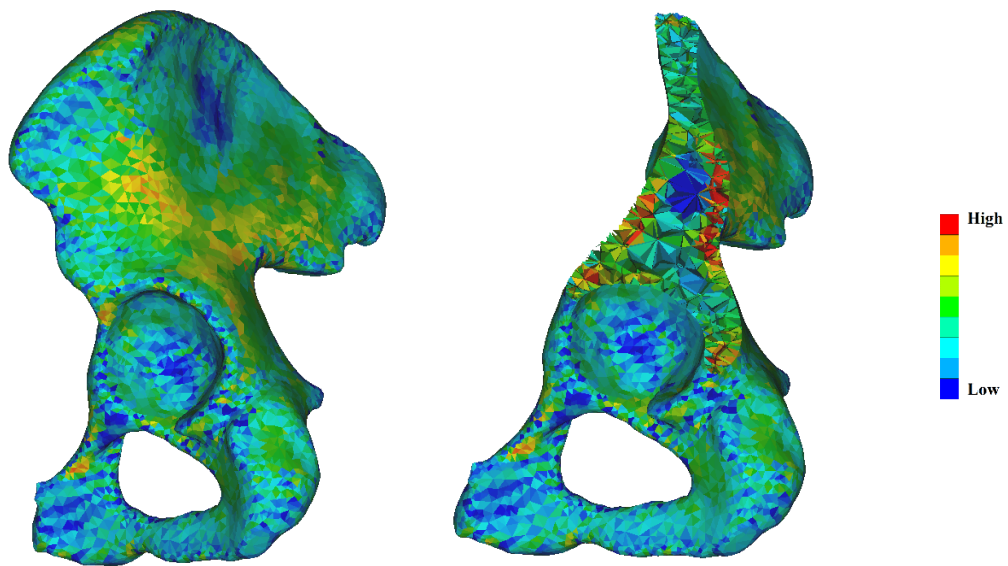


Figure 3.22 : Distribution of left pelvic material characteristics of healthy.

Table 3.9: Max, Min and Average of the density and E-Modulus of the left pelvic healthy model

	Density (g/cm^3)	E-Modulus (GPa)
Max	1,876	9,523
Median	1,462	2,615
Min	1,047	0,187

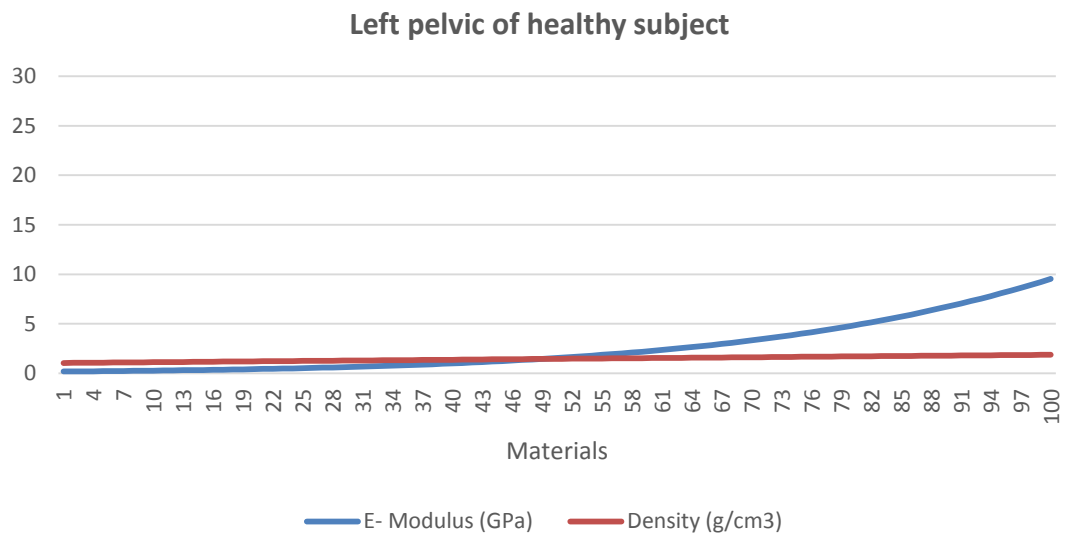


Figure 3.23 : Density and E-Modulus distribution on material numbers.

3.5 Boundary Conditions

The upper body weight is spread along the pelvic bone. At this time, the load on the vertebrae passes through the sacroiliac joint to the pelvis. Since the pelvis is divided into two pieces, this load is scattered and passes through the femur with acetabular. The pelvic bone is connected to the pubic symphysis by the cartilage. Femur and acetabular have a contact surface via cartilage with each other. There is load transfer through these surfaces. The researchers used fixed support to determine boundary conditions in studies where two surfaces with negligible motion or friction were connected to each other [65]. However, if the friction between the two tissues is low, the frictionless support is preferred. This study used fixed support in sacroiliac joint and frictionless support in pubis symphysis. Supported parts of the bones are manually identified by the face selection operator. Figure 3.24 shows the selected faces for the boundary conditions. When selecting faces, the contact points of the 3D model obtained from the CT image of the patient were taken into account.

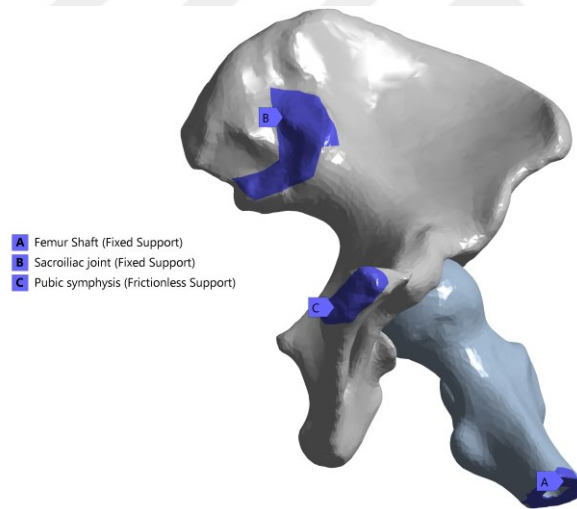


Figure 3.24 : Boundary conditions for pelvic (A and B surface is fixed support, C surface is frictionless support).

3.6 Boundary Conditions: Loading

The loads applied to the femur vary according to the daily activities. Various loads occur on the acetabular surface in cases such as walking, standing, running and weight lifting. The individual's own weight plays an important role in the resulting loads. However, since the patient's data was anonymized, weight data could not be used.

Therefore, the patient's weight was compared to previous studies and an approximated value was determined [66]. Force directions and magnitudes were calculated. In addition, the high force was applied to create sideways acetabular fractures [67-68]. The applied forces are shown in Table 3.10. The analysis was performed on femur according to the directions and magnitudes selected and it was aimed to measure acetabular stresses (Figure 3.25).

Table 3.10 : Magnitude of the applied force

Conditions	FORCE (N)
During normal walking	250
During standing	370
Sideways fracture	2000, 9000

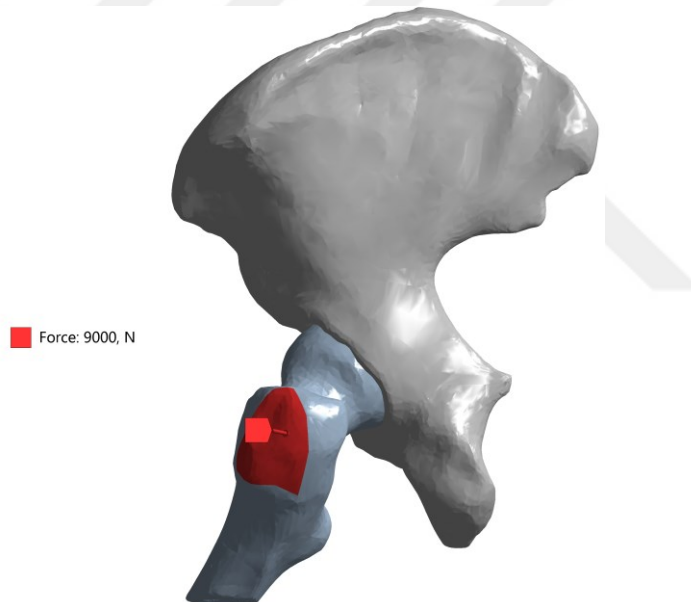


Figure 3.25 : The force applied to the femur.

3.7 Cortical Thickness

The cortical thickness decreases due to aging. It may contain information about the patient's fractured bone [69]. As the cortical thickness of the person decreases, the risk of bone fracture increases. Therefore, cortical thicknesses of young and old were investigated in this study. To find the cortical thickness, it is measured using the pixel spacing value with the aid of the MATLAB. In the CT image, the cortical bone is more whiter than the trabecular bone. The length of the white section gives a cortical

thickness. In order to calculate this, the threshold value was determined so that the cortical regions were visible in the CT image. The cortical structure was shown by assigning 0 values to the pixels below the selected threshold value in the CT image. A CT sections were selected where the acetabulum pit was seen clearly (Figure 3.26). Using the pixel spacing value from DICOM, the distance between 2 points was calculated. Calculations were made from many different points and the maximum and minimum values were found. The cortical thickness was found to be varying between 2.395 and 4.011 mm in the acetabulum for the healthy subject. On the other hand, cortical thickness of the patient with acetabular fracture was found to be varying between 2.203 and 2.257 mm.

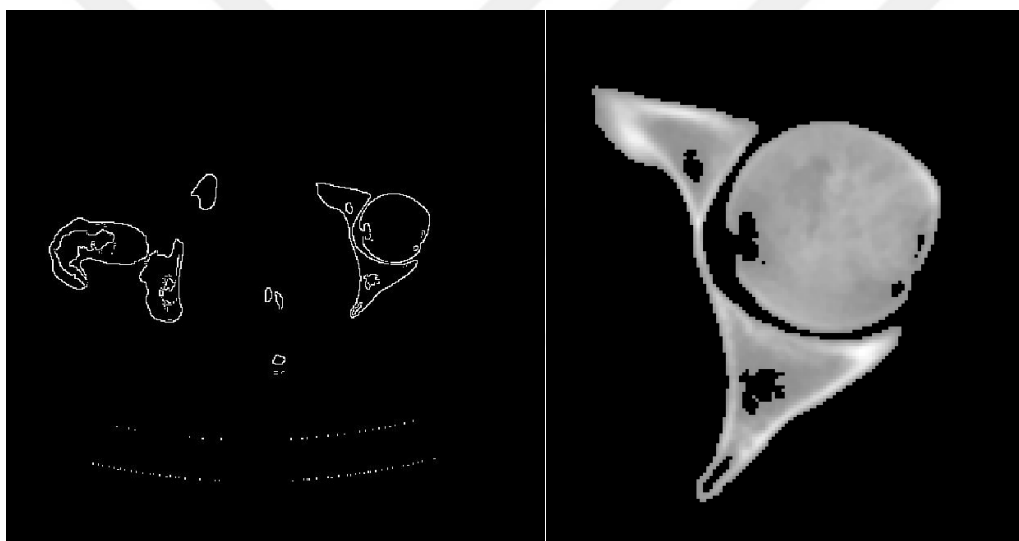
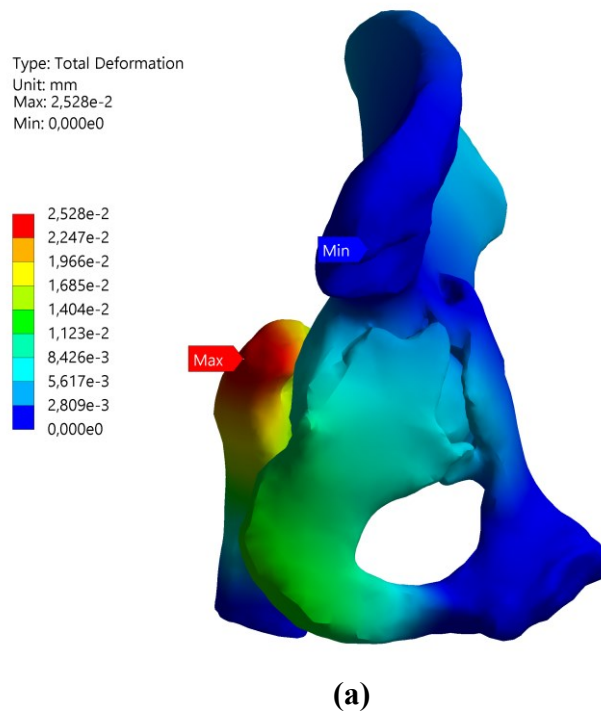


Figure 3.26 : Cleaning trabecular bone for calculating cortical thickness in a slice

After the 3D model was created, the material properties of the 3D models were obtained by utilizing the HU values. The elastic modulus of the elderly patient with acetabular fracture was found to be lower than the other healthy subject. The boundary conditions were determined by using the information in the literature and various forces were applied. The inputs for the analysis were prepared and the model was created successfully.

4. RESULTS

In this study, the relationship between the healthy subject and the patient with fracture was investigated and the mechanism of the fracture was examined. There were differences in the FEA, cortical thickness and material properties between the patient with a fracture and healthy subject. The deformation of an object due to the influence of various internal and external forces is called total deformation. Total deformations were examined to observe the difference between the model with a fracture and the model with the healthy model. The numerical distributions of the analysis results in each figure are shown in color. As the color scale, the numerical values increased from blue to red. For each FE model, the figures of the femoral and pelvic bones are shown first. In the other figures, in order to show the distribution at the junction points of the bones, each bone is hidden separately. The results of the analysis are shown in Figures 4.1, 4.2, 4.3, and 4.4. Total deformation, von-Mises and Strain results are given in Tables 4.1, 4.2, 4.3, 4.4, and 4.5 for each model.



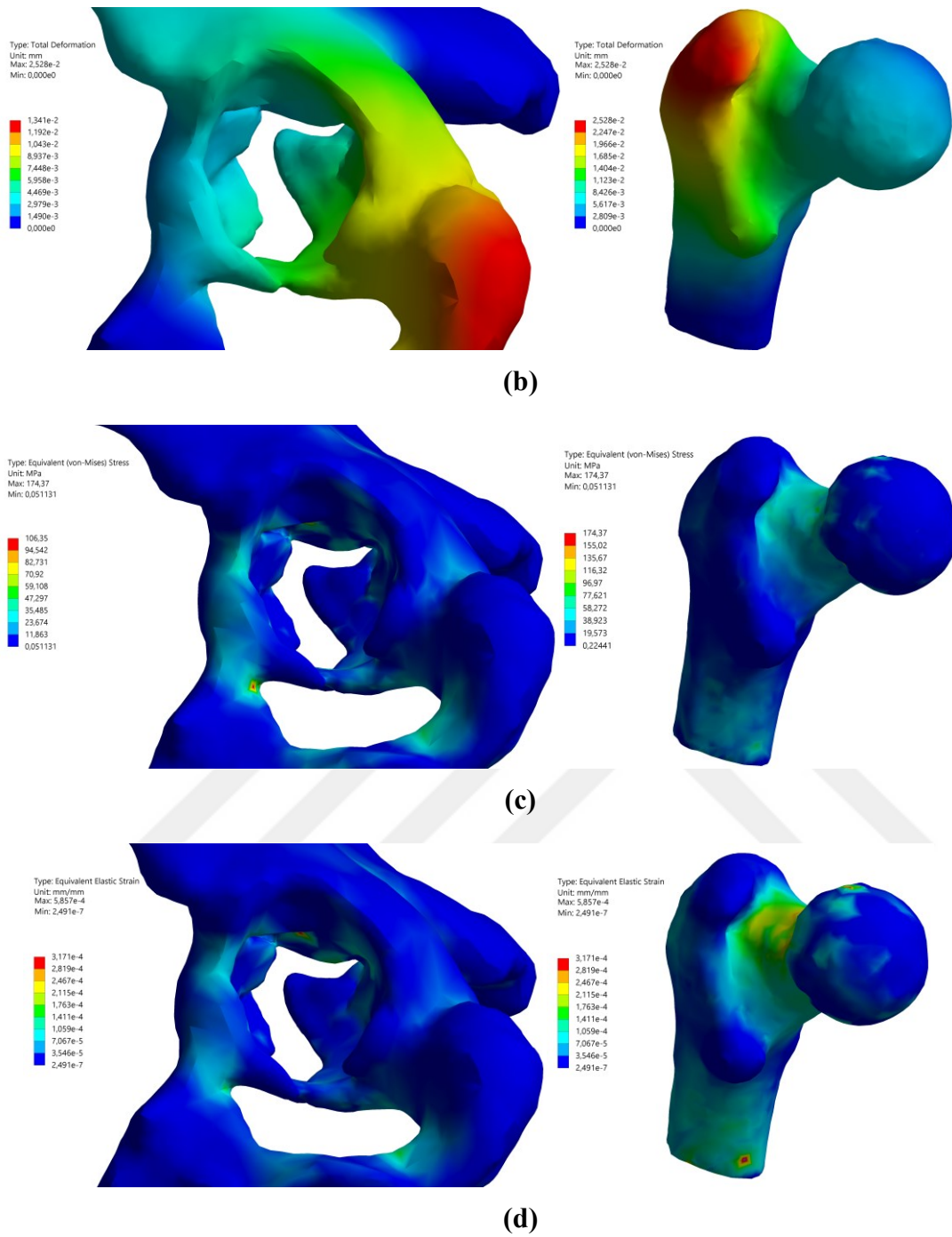
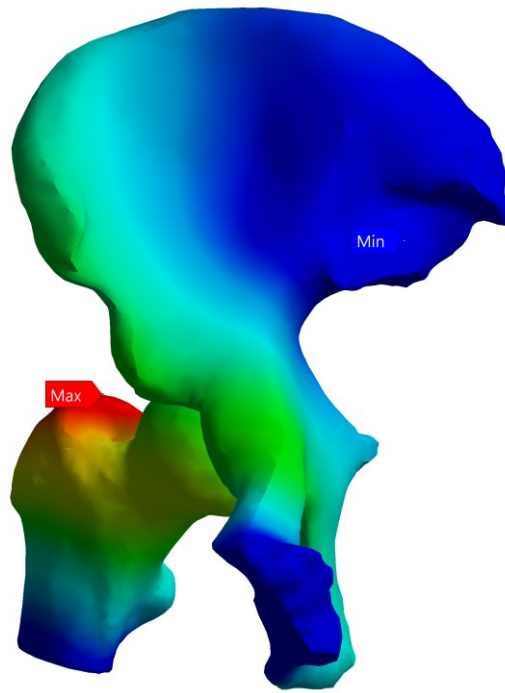
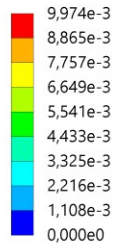


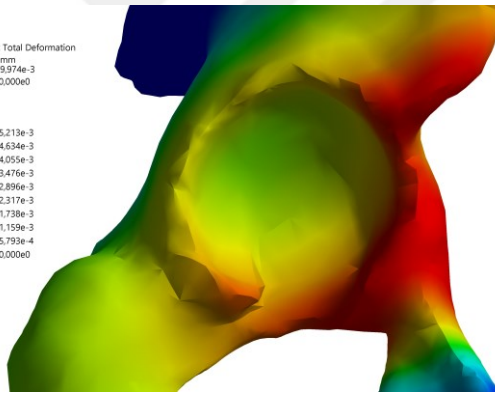
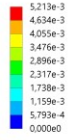
Figure 4.1 : Analysis of the left model of the patient with a fracture, **(a)** Total deformation, **(b)** Total deformation for each model, **(c)** Equivalent (von-Mises) Stress for each model, **(d)** Equivalent Elastic Strain for each model

Type: Total Deformation
Unit: mm
Max: 9,974e-3
Min: 0,000e0



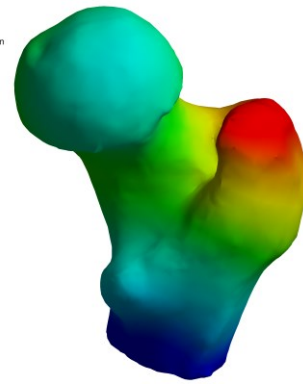
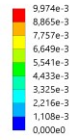
(a)

Type: Total Deformation
Unit: mm
Max: 9,974e-3
Min: 0,000e0

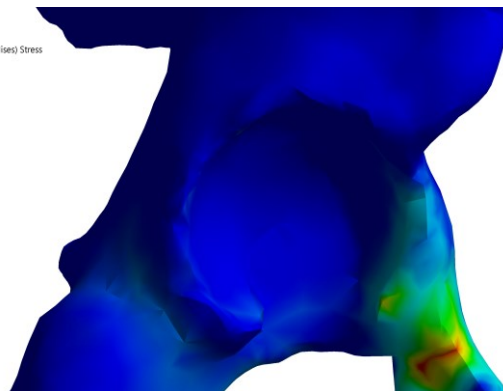
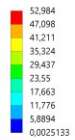


(b)

Type: Total Deformation
Unit: mm
Max: 9,974e-3
Min: 0,000e0

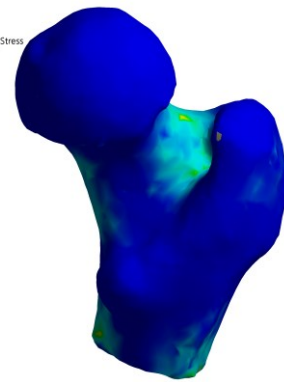
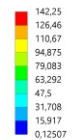


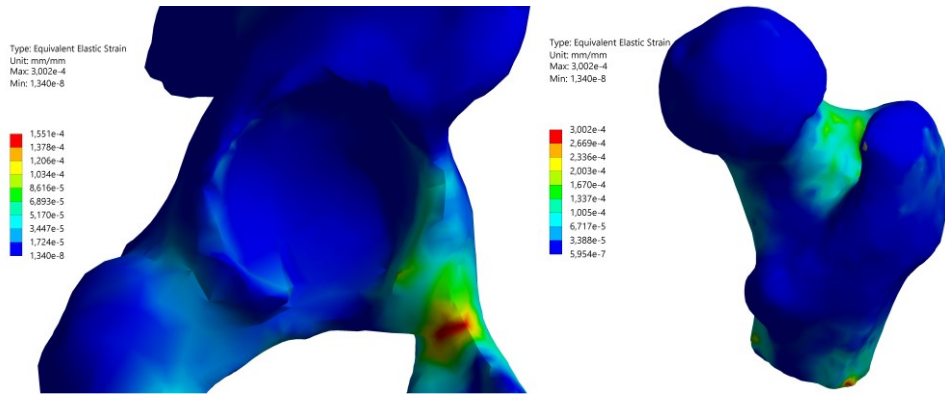
Type: Equivalent (von-Mises) Stress
Unit: MPa
Max: 142,25
Min: 0,0025133



(c)

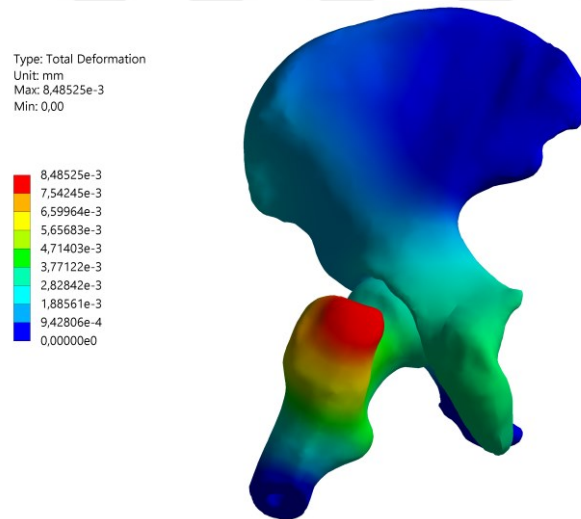
Type: Equivalent (von-Mises) Stress
Unit: MPa
Max: 142,25
Min: 0,0025133



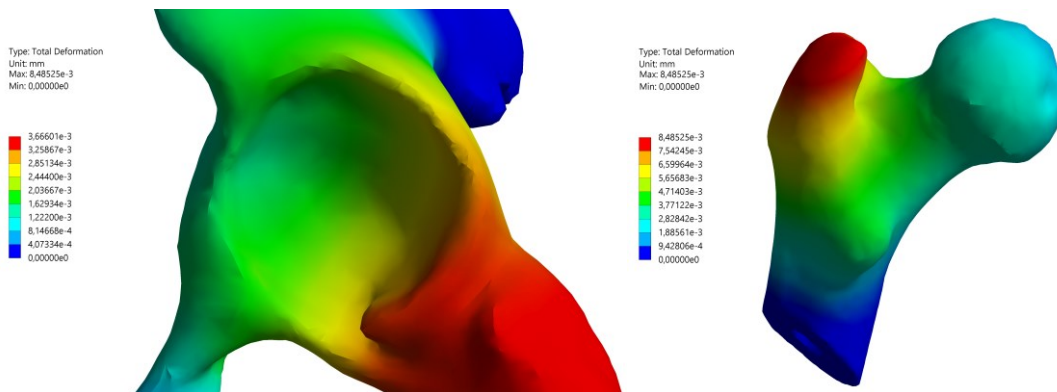


(d)

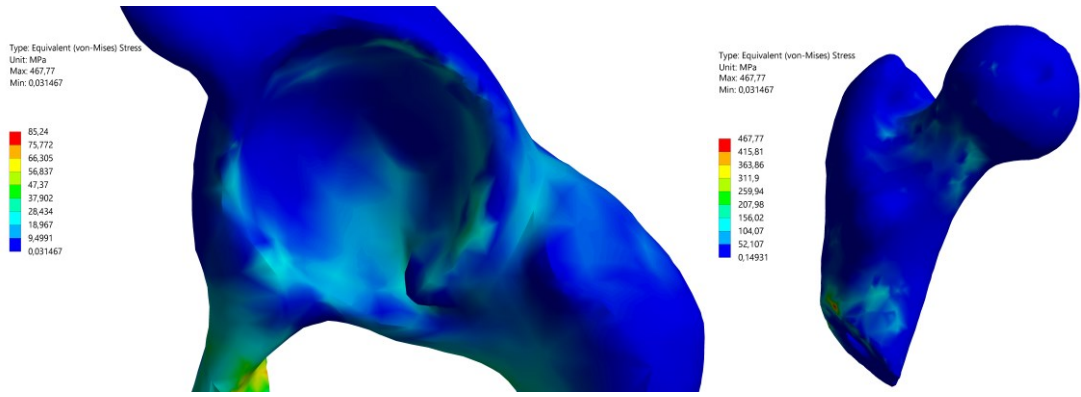
Figure 4.2 : Analysis of the right model of the patient with a fracture, (a) Total deformation, (b) Total deformation for each model, (c) Equivalent (von-Mises) Stress for each model, (d) Equivalent Elastic Strain for each model



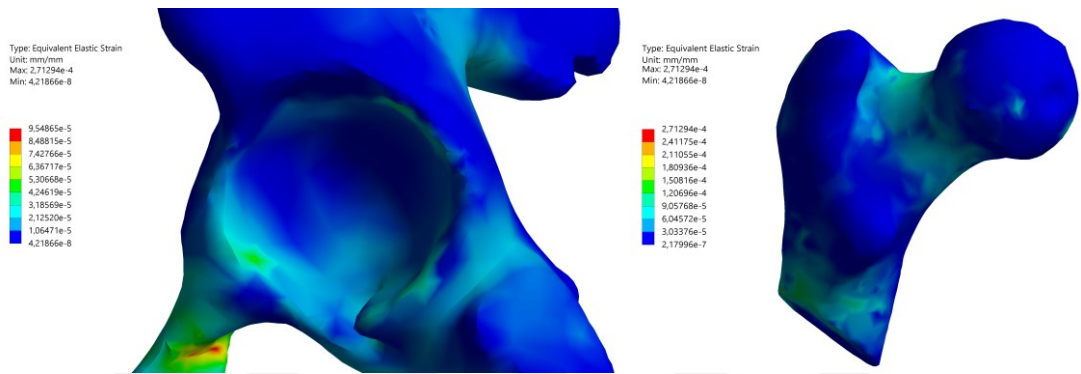
(a)



(b)

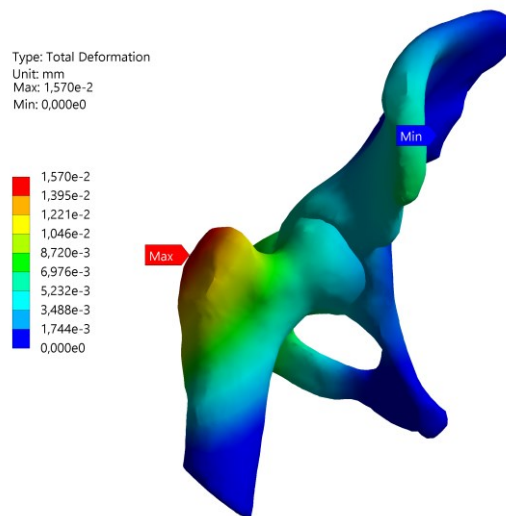


(c)

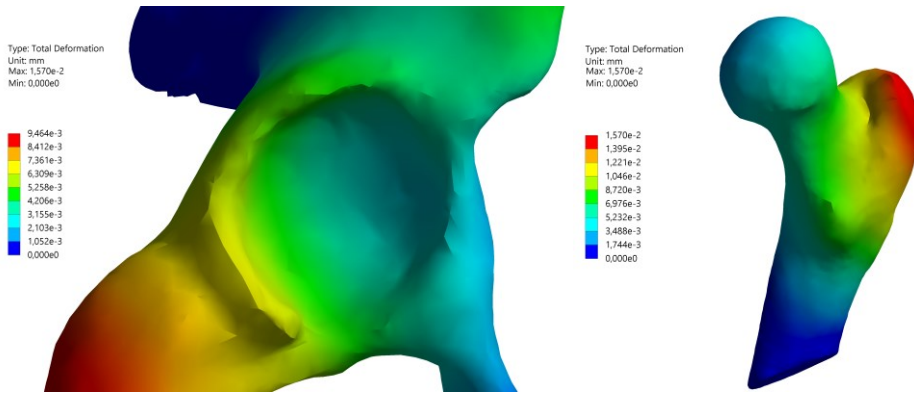


(d)

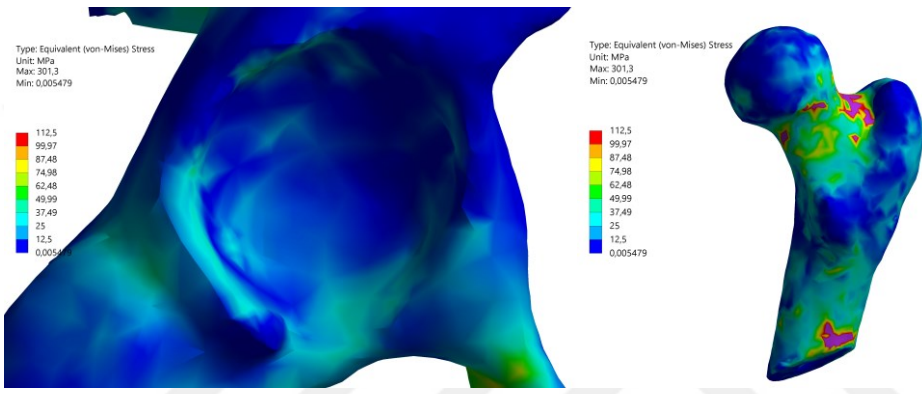
Figure 4.3 : Analysis of the left model of the healthy subject, (a) Total deformation (b) Total deformation for each model, (c) Equivalent (von-Mises) Stress for each model, (d) Equivalent Elastic Strain for each model



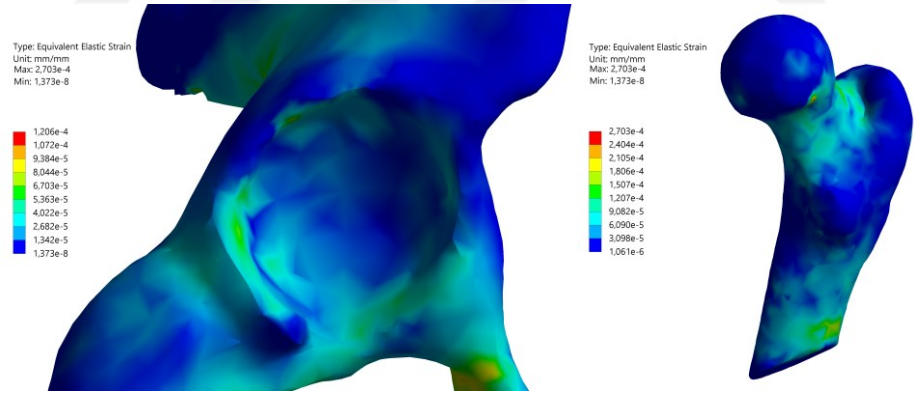
(a)



(b)



(c)



(d)

Figure 4.4 : Analysis of the right model of the healthy subject, **(a)** Total deformation, **(b)** Total deformation for each model, **(c)** Equivalent (von-Mises) Stress for each model, **(d)** Equivalent Elastic Strain for each model

These figures were created by taking screenshots from the software only when 9000N force is applied. The results of the other forces were not given as figures because the distributions did not change. The following tables show the results for different force

loading. In this study, three outputs were taken into consideration for analysis results. These are total deformation, von-Mises and strain.

Table 4.1: Total deformation, von-Mises and Strain results of the left model with a fracture.

Force	9000N		2000N		370N		250N	
	Max	Min	Max	Min	Max	Min	Max	Min
Total Deformation (mm)	2,53 $\times 10^{-2}$	0	5,62 $\times 10^{-3}$	0	1,04 $\times 10^{-3}$	0	7,02 $\times 10^{-4}$	0
von Mises (MPa)	174,37	0,051	38,748	0,011	7,168	0,002	4,843	0,001
Strain	5,86 $\times 10^{-4}$	2,49 $\times 10^{-7}$	1,30 $\times 10^{-4}$	5,54 $\times 10^{-8}$	2,41 $\times 10^{-5}$	1,02 $\times 10^{-8}$	1,63 $\times 10^{-5}$	6,92 $\times 10^{-9}$

Table 4.2: Total deformation, von Mises and Strain results of the right model with a fracture.

Force	9000N		2000N		370N		250N	
	Max	Min	Max	Min	Max	Min	Max	Min
Total Deformation (mm)	1,005 $\times 10^{-2}$	0	2,23 $\times 10^{-3}$	0	4,12 $\times 10^{-4}$	0	2,78 $\times 10^{-4}$	0
von Mises (MPa)	142,25	0,12507	31,611	0	5,848	0	3,954	0
Strain	3,02 $\times 10^{-4}$	5,95 $\times 10^{-7}$	6,70 $\times 10^{-5}$	3,11 $\times 10^{-9}$	1,24 $\times 10^{-5}$	5,76 $\times 10^{-10}$	8,38 $\times 10^{-6}$	0

Table 4.3: Total deformation, von Mises and Strain results of the left model (the healthy subject).

Force	9000N		2000N		370N		250N	
	Max	Min	Max	Min	Max	Min	Max	Min
Total Deformation (mm)	8,49 $\times 10^{-3}$	0	1,89 $\times 10^{-3}$	0	3,49 $\times 10^{-4}$	0	2,36 $\times 10^{-4}$	0
von Mises (MPa)	467,77	0,03	103,95	0,006	19,231	0,001	12,994	0
Strain	2,71 $\times 10^{-4}$	4,22 $\times 10^{-8}$	6,03 $\times 10^{-5}$	9,37 $\times 10^{-9}$	1,12 $\times 10^{-5}$	1,73 $\times 10^{-9}$	7,54 $\times 10^{-6}$	1,17 $\times 10^{-9}$

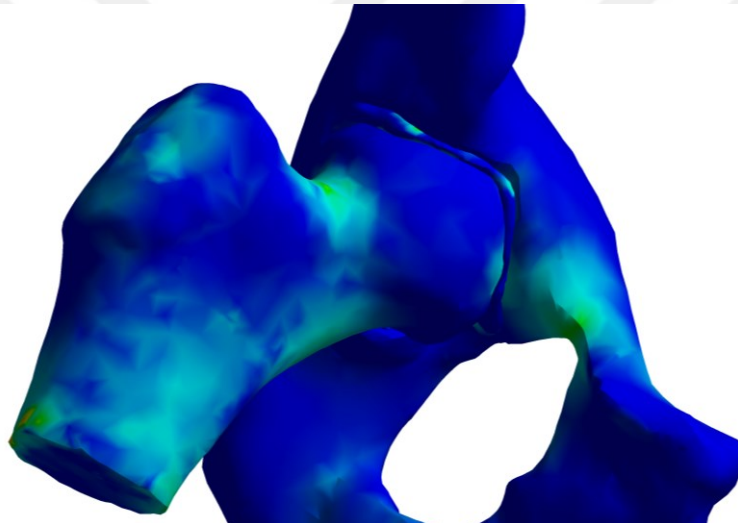
Table 4.4: Total deformation, von Mises and Strain results of the right model (the healthy subject).

Force	9000N		2000N		370N		250N	
	Max	Min	Max	Min	Max	Min	Max	Min
Total Deformation (mm)	1,57 $\times 10^{-3}$	0	3,49 $\times 10^{-3}$	0	6,45 $\times 10^{-4}$	0	4,36 $\times 10^{-4}$	0
von Mises (MPa)	301,27	0,721	66,949	0,16	12,386	0,029	8,367	0,02
Strain	2,70 $\times 10^{-4}$	1,07 $\times 10^{-6}$	6,01 $\times 10^{-5}$	2,36 $\times 10^{-7}$	1,11 $\times 10^{-5}$	4,36 $\times 10^{-8}$	7,50 $\times 10^{-6}$	2,95 $\times 10^{-8}$

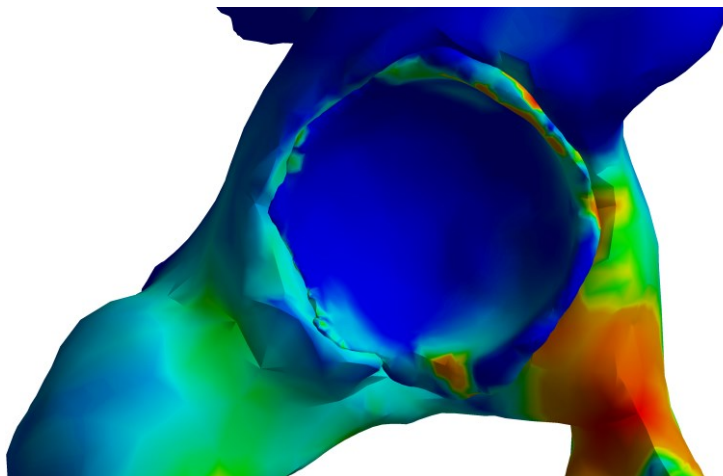
Table 4.5: Total deformation, von-Mises and Strain results of the right model with a fracture (includes articular cartilage).

Force	9000N		2000N	
	Max	Min	Max	Min
Total Deformation (mm)	$9,68 \times 10^{-3}$	0	$2,15 \times 10^{-3}$	0
von Mises (MPa)	141,59	0,002	31,46	0
Strain	$3,04 \times 10^{-4}$	$8,89 \times 10^{-9}$	$6,75 \times 10^{-5}$	$1,95 \times 10^{-9}$

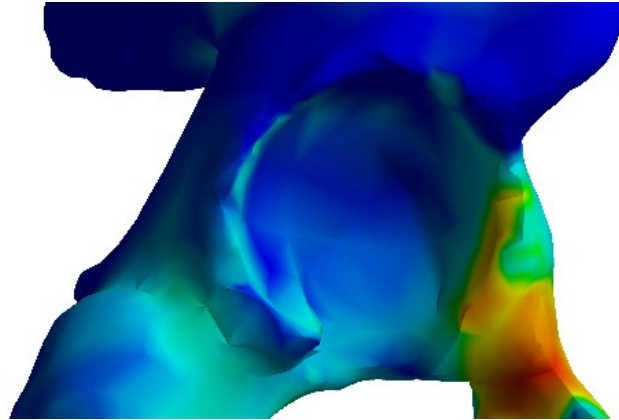
Strain distribution of articular cartilage model is shown in Figure 4.5(a)(b). The FE analysis of the same model was solved without cartilage. Strain distribution of this model is shown in Figure 4.5(c).



(a)



(b)



(c)

Figure 4.5 : (a) The right model with a fracture (includes articular cartilage), (b) Femur is hidden to show the distribution of strain, (c) The right model without articular cartilage

The fracture propagation was investigated by using the right model with a fracture. The points where the strain increased were chosen and the fracture path was formed (Figure 4.6).

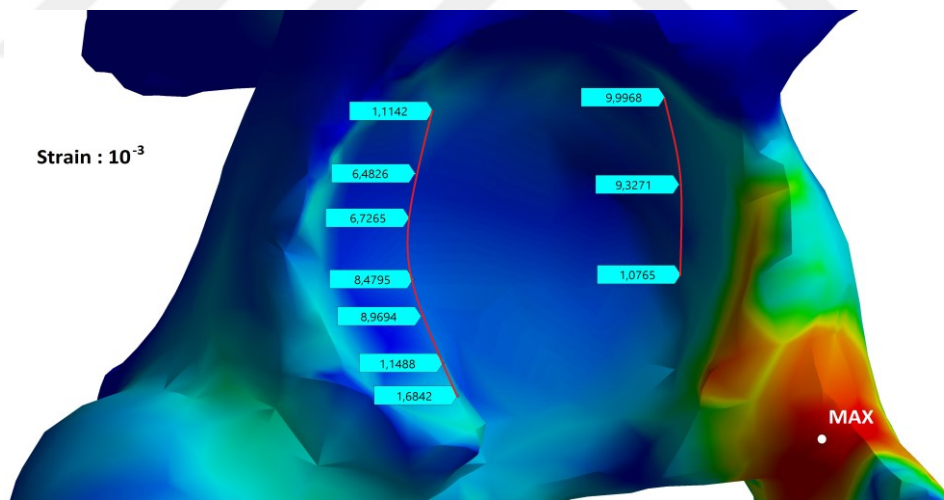


Figure 4.6 : Probable fracture path estimation of the right model with a fracture



5. DISCUSSION

In terms of material characteristics, the maximum Young's modulus of the right femur of the fractured patient was found to be 16 GPa and the left femur was 20 GPa. In contrast, the right femur Young's modulus of the healthy subject was found to be maximum 25 GPa. It was determined that the values of Young's modulus of the healthy subject were higher. These results are similar to previous studies [70-71]. In addition to being age-related, the elastic modulus of the patient with fracture should be lower than the healthy subject [72]. The Poisson ratio was selected 0.3, similar to previous studies [73].

A significant difference was observed between the subject with a fracture and a healthy subject [74]. The von Mises values of the left and right models of the healthy subject were 467MPa and 301MPa, respectively, and these values were 174MPa and 142MPa, respectively, in the patient who had a fracture (Tables 4.1, 4.2, 4.3, and 4.4). It was concluded that healthy subject can be sustained higher loads. It is expected to be low von Mises stress of patient with a fracture. In addition, there was found a significant difference between the left and the right model of the patient with a fracture in terms of stress values. It was predicted that the right model could be fractured if exposed to any other low energy force because the left fracture model has a higher von Mises value than the right model. Total deformation of the patient with fracture was higher in both models than the healthy subject. In the subject with a fracture, the left model was observed to have higher deformation than the right. Total deformation on the left model was $2,53 \times 10^{-2}$ mm and the non-fractured right side was $1,005 \times 10^{-2}$ mm (Tables 4.1, and 4.2). Therefore, the FE model is verified to be correct for producing results in the expected ratios.

The articular cartilage between the femur and the acetabulum was modeled and the effect of FEA on the results was investigated. Since it is difficult to construct the cartilage model from the CT image, this was performed in one model. For this, the model used is the right model of the subject with fracture (Figure 3.6). According to

the results, the von Mises value was 141.59MPa in cartilage model and 142.25MPa without cartilage model (Tables 4.2, and 4.5). As the difference is small enough to be neglected, no separate cartilage model is formed for each model. As for stress distribution, it was shown that the distributions were not equal and were collected in one place in both models of the subject with a fracture (Figures 4.1, and 4.2). On the contrary, stress-strain values were shown to be evenly distributed for the healthy subject's models (Figures 4.3, and 4.4).

Determining the material properties was challenging for each model. Since the number of slices in the CT image is high, it took a half hour to calculate the material properties in MATLAB. Once the material properties were calculated, it was difficult to transfer this information to the ANSYS. Each bone model, femur and pelvis were contacted to each other. Therefore, it is necessary to introduce the material properties of each element of the two bones to the system. However, at ANSYS a material property can be specified for a single body, contrarily for this, each element of our bones has its own material properties. To overcome this problem, we had to write code via ANSYS Apdl. The geometry first transferred to the ANSYS creates the first body. The added body is the numbered sequentially. After the initial geometry is added, the material properties calculated for the second geometry must be added to the material properties of the first geometry. If two separate codes are written, it causes a conflict. Material properties should be entered by continuing from the last element numbering of the first geometry. The total number of material properties should be equal to the sum of the two bodies' material properties. Command line was created for the first geometry through ANSYS Apdl. Codes are given in the appendix. It has been tested whether the system reads the material properties or not and the results of the analysis are different when the material properties are added and not added.

The analysis was performed with 64 bit Windows 8.1 MSI Intel Core i7-4712MQ processor 2.3GHz, 8GB ram 2GB video card. The time spent on a model's analysis was 5-7 minutes.

6. CONCLUSIONS

Our motivation for this research, is to try to understand the low energy fractures in osteoporotic people. The prediction of possible fractures and ensuring that the patient and the surgeon to take the necessary precautions, have stimulated us to carry out this study.

CT images were obtained for two patients. One of these images belongs to an 88-year-old female patient with osteoporosis and fracture, while the other is a 24-year-old male without any fracture. After the CT images were converted to 3D model, various arrangements were made on the model. A total of 4 models were created for each patient, including right and left side. Additionally, in order to observe the effect of the articular cartilage between the femur and acetabular, cartilage model was added to the right model of the subject with a fracture. The material properties required for FEM were calculated from the HU value by using the formulas in the literature and the Young's modulus and apparent density were calculated. The calculated material properties and each model were transferred separately to the ANSYS and 4-noded tetrahedral meshing was performed. Using the literature, the forces were applied to the femur greater trochanter while the person was standing, walking and exposed to high forces. The direction of force was directed towards acetabulum and 9000N, 2000N, 370 and 250N forces were applied. When determining the direction of the applied force, the direction was chosen so as to create stress on the acetabular surface. Boundary conditions were examined in the literature, 2 fixed support and 1 frictionless support created (Figure 3.24). In addition, acetabular cortical thickness values in two different images were calculated and compared.

In this study, FEA was applied to the subject with osteoporosis and fracture, unlike other studies. The validation of this study could not be performed mechanically because there were no cadaveric bones. Instead, validation has been achieved by using the data available in the literature. Bones can be examined mechanically in the event that cadavers are found in the future or if people using CT images donate cadavers.

In this study, loads are selected to produce low energy fractures. A similar operation can be performed in high energy fractures. The applied force directions were determined approximately. Force directions can be examined by more accurate validation in other studies. The model has heterogeneous material properties. This has led to more accurate results. One of the missing features of our model is to select anisotropic material properties instead of orthotropic material properties. However, the model can be created homogeneously to simplify the model and save the calculation time. According to the analysis results, the cartilage between the femur and the acetabulum can be neglected.

This study inspired to analyze fracture estimates and to identify possible fracture conditions. The next stage of this study is to inform the patient about the possibility of fracture before the fracture. Studies have increased in this direction [75]. Especially in elderly and osteoporotic people, it can be prevented from bone fractures, which frequently occur and can result in death. Using the CT images of the patient, an automated FE model can be created via various software. With the FEM, artificial intelligence algorithms can be used to determine possible fracture conditions. In this study, we have investigated the acetabular fractures, which are usually fatal or have a difficult operation.

It is important to examine the acetabulum, which is a junction of the femur and pelvic bones and is filled with nerves. Therefore, preventing the formation of fracture will reduce both hospital costs and reduce injuries also morbidity due to complications. The FE model that we have created sheds a light on further studies. The disadvantage of this study is that the number of CT images is not sufficient. Images of 2 patients have been obtained due to the ethical processes and time-consuming FE models. If the system can be configured to be automated, time can be saved. Nowadays, deep learning that is quite popular can be used to create automated systems. This study was performed in a static structure. However, daily accidents are dynamic, dynamic models could be designed in FEM.

In this study, crack propagation was investigated in the right model of the patient with a fracture. If the operation is necessary and the implant is to be transplanted before the fracture, implant designs suitable for possible fracture path can be performed.

REFERENCES

- [1] Netter, F. H. (2017). *Atlas of Human Anatomy E-Book*. Philadelphia, PA : Elsevier Health Sciences.
- [2] Neuman, W. F., & Neuman, M. W. (1958). *The chemical dynamics of bone mineral*. Chicago, U.S. : The University of Chicago Press.
- [3] Dağistan S. (2016). Kemik Mineral Yoğunluk Ölçüm Yöntemleri ve Dış Hekimliği. *Turkiye Klinikleri Oral and Maxillofacial Radiology*, 2(1), 71-7.
- [4] Peng, L., Bai, J., Zeng, X., & Zhou, Y. (2006). Comparison of isotropic and orthotropic material property assignments on femoral finite element models under two loading conditions. *Medical Engineering & Physics*, 28(3), 227-233.
- [5] Baca, V., Horak, Z., Mikulenka, P., & Dzupa, V. (2008). Comparison of an inhomogeneous orthotropic and isotropic material models used for FE analyses. *Medical Engineering & Physics*, 30(7), 924-930.
- [6] Bessho, M., Ohnishi, I., Matsuyama, J., Matsumoto, T., Imai, K., & Nakamura, K. (2007). Prediction of strength and strain of the proximal femur by a CT-based finite element method. *Journal of Biomechanics*, 40(8), 1745-1753.
- [7] Yosibash, Z., Padan, R., Joscowicz, L., & Milgrom, C. (2007). A CT-based high-order finite element analysis of the human proximal femur compared to in-vitro experiments. *Journal of Biomechanical Engineering*, 129(3), 297-309.
- [8] Rohlmann, A., Mössner, U., Bergmann, G., & Kölbl, R. (1982). Finite-element-analysis and experimental investigation of stresses in a femur. *Medical Engineering and Physics*, 4(3), 241-246.
- [9] Klues, D. (2010). *Finite element analysis in orthopaedic biomechanics*. Rostock, Germany : IntechOpen.
- [10] Diamantopoulos, A. P., Rohde, G., Johnsrud, I., Skoie, I. M., Hochberg, M., & Haugeberg, G. (2012). The epidemiology of low-and high-energy distal radius fracture in middle-aged and elderly men and women in Southern Norway. *PLoS One*, 7(8), e43367.
- [11] Radasch, R. M. (1999). Biomechanics of bone and fractures. *Veterinary Clinics: Small Animal Practice*, 29(5), 1045-1082.
- [12] Natali, A. N., & Meroi, E. A. (1989). A review of the biomechanical properties of bone as a material. *Journal of Biomedical Engineering*, 11(4), 266-276.
- [13] Dalstra, M., Huiskes, R., & Van Erning, L. (1995). Development and validation of a three-dimensional finite element model of the pelvic bone. *Journal of Biomechanical Engineering*, 117(3), 272-278.
- [14] Anderson, A. E., Peters, C. L., Tuttle, B. D., & Weiss, J. A. (2005). Subject-specific finite element model of the pelvis: development, validation and sensitivity studies. *Journal of Biomechanical Engineering*, 127(3), 364-373.
- [15] Silva, M. E. T., Brandão, S., Parente, M. P. L., Mascarenhas, T., & Natal Jorge, R. M. (2017). Biomechanical properties of the pelvic floor muscles of continent and incontinent women using an inverse finite element analysis. *Computer Methods in Biomechanics and Biomedical Engineering*, 20(8), 842-852.

- [16] Ghosh, R., Pal, B., Ghosh, D., & Gupta, S. (2015). Finite element analysis of a hemi-pelvis: the effect of inclusion of cartilage layer on acetabular stresses and strain. *Computer Methods in Biomechanics and Biomedical Engineering*, 18(7), 697-710.
- [17] Phillips, A. T. M., Pankaj, P., Howie, C. R., Usmani, A. S., & Simpson, A. H. R. W. (2007). Finite element modelling of the pelvis: inclusion of muscular and ligamentous boundary conditions. *Medical Engineering & Physics*, 29(7), 739-748.
- [18] Viceconti, M., Bellingeri, L., Cristofolini, L., & Toni, A. (1998). A comparative study on different methods of automatic mesh generation of human femurs. *Medical Engineering & Physics*, 20(1), 1-10.
- [19] Clarke, B. (2008). Normal bone anatomy and physiology. *Clinical Journal of the American Society of Nephrology*, 3(3), 131-139.
- [20] Bonewald, L. F. (2011). The amazing osteocyte. *Journal of Bone and Mineral Research*, 26(2), 229-238.
- [21] Sims, N. A., & Gooi, J. H. (2008). Bone remodeling: Multiple cellular interactions required for coupling of bone formation and resorption. *In Seminars in Cell & Developmental Biology*, 19(5), 444-451.
- [22] Buckwalter, J. A., Glimcher, M. J., Cooper, R. R., & Recker, R. (1996). Bone biology. I: Structure, blood supply, cells, matrix, and mineralization. *Journal of Bone and Joint Surgery-American Volume*, 77(8), 1256-1275.
- [23] Downey, P. A., & Siegel, M. I. (2006). Bone biology and the clinical implications for osteoporosis. *Physical Therapy*, 86(1), 77-91.
- [24] Capulli, M., Paone, R., & Rucci, N. (2014). Osteoblast and osteocyte: games without frontiers. *Archives of Biochemistry and Biophysics*, 561, 3-12.
- [25] Crockett, J. C., Mellis, D. J., Scott, D. I., & Helfrich, M. H. (2011). New knowledge on critical osteoclast formation and activation pathways from study of rare genetic diseases of osteoclasts: focus on the RANK/RANKL axis. *Osteoporosis International*, 22(1), 1-20.
- [26] Franz-Odenaal, T. A., Hall, B. K., & Witten, P. E. (2006). Buried alive: how osteoblasts become osteocytes. *Developmental Dynamics*, 235(1), 176-190.
- [27] Dallas, S. L., Prideaux, M., & Bonewald, L. F. (2013). The osteocyte: an endocrine cell... and more. *Endocrine Reviews*, 34(5), 658-690
- [28] Miller, S. C., de Saint-Georges, L., Bowman, B. M., & Jee, W. S. (1989). Bone lining cells: structure and function. *Scanning Microscopy*, 3(3), 953-60.
- [29] Robling, A. G., Castillo, A. B., & Turner, C. H. (2006). Biomechanical and molecular regulation of bone remodeling. *Annual Review of Biomedical Engineering*, 8, 455-498.
- [30] Florencio-Silva, R., Sasso, G. R. D. S., Sasso-Cerri, E., Simões, M. J., & Cerri, P. S. (2015). Biology of bone tissue: structure, function, and factors that influence bone cells. *BioMed Research International*, 2015, 1-17.
- [31] Burkitt, H. G., Young, B., & Hath, J. W. (1993). *Wheater's functional histology: a text and colour atlas*. Hong Kong, China: Longmann Group.
- [32] Cross-section of bone. (2018, October 15). Retrieved from <https://en.wikipedia.org/wiki/Bone>
- [33] Kanis, J. A., Melton III, L. J., Christiansen, C., Johnston, C. C., & Khaltaev, N. (1994). The diagnosis of osteoporosis. *Journal Of Bone and Mineral Research*, 9(8), 1137-1141.

- [34] Moore, K. L., Dalley, A. F., & Agur, A. M. (2013). *Clinically oriented anatomy*. Philadelphia, PA: Lippincott Williams & Wilkins.
- [35] Pagenkopf, E., Grose, A., Partal, G., & Helfet, D. L. (2006). Acetabular Fractures in the Elderly: Treatment Recommendations. *HSS Journal*, 2(2), 161-171.
- [36] Good, D. W., Leonard, M., Lui, D., Morris, S., & McElwain, J. P. (2011). Acetabular fractures following rugby tackles: a case series. *Journal of Medical Case Reports*, 5(1), 505.
- [37] Mears, D. C., & Velyvis, J. H. (2002). Acute total hip arthroplasty for selected displaced acetabular fractures: two to twelve-year results. *The Journal of Bone & Joint Surgery*, 84(1), 1-9.
- [38] Lowe, J. A., Pearson, J., Leslie, M., & Griffin, R. (2018). Ten-Year Incidence of High-Energy Geriatric Trauma at a Level 1 Trauma Center. *Journal of Orthopaedic Trauma*, 32(3), 129-133.
- [39] Peitzman, A. B., Fabian, T. C., Rhodes, M., Yealy, D. M., & Schwab, C. W. (Eds.). (2012). *The trauma manual: trauma and acute care surgery*. Lippincott Williams & Wilkins.
- [40] Evans, J. A., van Wessel, K. J., McDougall, D., Lee, K. A., Lyons, T., & Balogh, Z. J. (2010). Epidemiology of traumatic deaths: comprehensive population-based assessment. *World Journal of Surgery*, 34(1), 158.
- [41] Pagenkopf, E., Grose, A., Partal, G., & Helfet, D. L. (2006). Acetabular fractures in the elderly: treatment recommendations. *HSS Journal*, 2(2), 161-171.
- [42] Barrett, H. H., & Swindell, W. (1996). *Radiological imaging: the theory of image formation, detection, and processing*. California, USA : Academic Press.
- [43] Szabo, B. A., & BabuÅška, I. (1991). *Finite element analysis*. Canada: John Wiley & Sons.
- [44] Hughes, T. J. (2012). *The finite element method: linear static and dynamic finite element analysis*. Englewood Cliffs, NJ : Courier Corporation.
- [45] Berkley, J., Weghorst, S., Gladstone, H., Raugi, G., Berg, D., & Ganter, M. (1999). Fast finite element modeling for surgical simulation. *Studies in Health Technology and Informatics*, 62, 55-61.
- [46] Strang, G., & Fix, G. J. (1973). *An analysis of the finite element method*. Englewood Cliffs, NJ: Prentice-hall.
- [47] Hutton, D. V., & Wu, J. (2004). *Fundamentals of finite element analysis*. New York, NY: McGraw-hill.
- [48] Brenner, S., & Scott, R. (2007). *The mathematical theory of finite element methods*. New York, NY : Springer Science & Business Media.
- [49] Zienkiewicz, O. C., & Taylor, R. L. (2000). *The finite element method: solid mechanics*. Barcelona, Spain : Butterworth-heinemann.
- [50] Zienkiewicz, O. C., & Taylor, R. L. (2005). *The finite element method for solid and structural mechanics*. Oxford, UK : Butterworth-heinemann.
- [51] Hooke, R. (1931). *Lectures de potentia restitutiva, or of spring explaining the power of springing bodies*. London,UK : John Martyn.
- [52] Mises, R. V. (1913). Mechanik der festen Körper im plastisch-deformablen Zustand. *Nachrichten von der Gesellschaft der Wissenschaften zu Göttingen, Mathematisch-Physikalische Klasse*, 1913(4), 582-592.
- [53] Cook, R. D., Malkus, D. S., Plesha, M. E., & Witt, R. J. (1974). *Concepts and applications of finite element analysis*. New York, NY: Wiley.
- [54] Most usual 3D elements. (2018, October 20). Retrieved From

- <http://illustrations.marin.ntnu.no/structures/analysis/FEM/theory/index.html>
- [55] Huiskes, R., & Chao, E. Y. S. (1983). A survey of finite element analysis in orthopedic biomechanics: the first decade. *Journal of Biomechanics*, 16(6), 385-409.
- [56] Zannoni, C., Mantovani, R., & Viceconti, M. (1999). Material properties assignment to finite element models of bone structures: a new method. *Medical Engineering & Physics*, 20(10), 735-740.
- [57] Cattaneo, P. M., Dalstra, M., & Frich, L. H. (2001). A three-dimensional finite element model from computed tomography data: a semi-automated method. *Proceedings of the Institution of Mechanical Engineers, Part H: Journal of Engineering in Medicine*, 215(2), 203-212.
- [58] Kim, J. H., & Paulino, G. H. (2002). Isoparametric graded finite elements for nonhomogeneous isotropic and orthotropic materials. *Journal of Applied Mechanics*, 69(4), 502-514.
- [59] Koivumäki, J. E., Thevenot, J., Pulkkinen, P., Kuhn, V., Link, T. M., Eckstein, F., & Jämsä, T. (2012). Ct-based finite element models can be used to estimate experimentally measured failure loads in the proximal femur. *Bone*, 50(4), 824-829.
- [60] Peng, L., Bai, J., Zeng, X., & Zhou, Y. (2006). Comparison of isotropic and orthotropic material property assignments on femoral finite element models under two loading conditions. *Medical Engineering & Physics*, 28(3), 227-233.
- [61] Anisotropic materials. (2018, October 25). Retrieved From <https://www.comsol.com/blogs/modeling-bone-strength-using-isotropic-anisotropic-materials/>
- [62] Cody, D. D., Gross, G. J., Hou, F. J., Spencer, H. J., Goldstein, S. A., & Fyhrie, D. P. (1999). Femoral strength is better predicted by finite element models than QCT and DXA. *Journal of Biomechanics*, 32(10), 1013-1020.
- [63] Shim, V. B., Pitto, R. P., Streicher, R. M., Hunter, P. J., & Anderson, I. A. (2008). Development and validation of patient-specific finite element models of the hemipelvis generated from a sparse CT data set. *Journal of Biomechanical Engineering*, 130(5), 051010.
- [64] Cilingir, A. C., Ucar, V., & Kazan, R. (2007). Three-dimensional anatomic finite element modelling of hemi-arthroplasty of human hip joint. *Trends Biomater Artif Organs*, 21(1), 63-72.
- [65] Ghosh, R., Pal, B., Ghosh, D., & Gupta, S. (2015). Finite element analysis of a hemi-pelvis: the effect of inclusion of cartilage layer on acetabular stresses and strain. *Computer Methods in Biomechanics and Biomedical Engineering*, 18(7), 697-710.
- [66] Bergmann, G., Deuretzbacher, G., Heller, M., Graichen, F., Rohlmann, A., Strauss, J., & Duda, G. N. (2001). Hip contact forces and gait patterns from routine activities. *Journal of Biomechanics*, 34(7), 859-871.
- [67] Olson, S. A., Bay, B. K., Chapman, M. W., & Sharkey, N. A. (1995). Biomechanical consequences of fracture and repair of the posterior wall of the acetabulum. *The Journal of Bone and Joint Surgery*, 77(8), 1184-1192.
- [68] Tile, M. (1988). Pelvic ring fractures: should they be fixed?. *The Journal of Bone and Joint Surgery*. British volume, 70(1), 1-12.

- [69] Treece, G. M., Gee, A. H., Mayhew, P. M., & Poole, K. E. (2010). High resolution cortical bone thickness measurement from clinical CT data. *Medical Image Analysis*, 14(3), 276-290.
- [70] Hodgskinson, R., & Currey, J. D. (1990). Effects of structural variation on Young's modulus of non-human cancellous bone. *Proceedings of the Institution of Mechanical Engineers, Part H: Journal of Engineering in Medicine*, 204(1), 43-52.
- [71] Burstein, A. H., Reilly, D. T., & Martens, M. (1976). Aging of bone tissue: mechanical properties. *The Journal of Bone and Joint Surgery. American Volume*, 58(1), 82-86.
- [72] Reilly, D. T., Burstein, A. H., & Frankel, V. H. (1974). The elastic modulus for bone. *Journal of Biomechanics*, 7(3), 271-275.
- [73] Ramos, A., & Simoes, J. A. (2006). Tetrahedral versus hexahedral finite elements in numerical modelling of the proximal femur. *Medical Engineering & Physics*, 28(9), 916-924.
- [74] Van Rietbergen, B., Huiskes, R., Eckstein, F., & R egsegger, P. (2003). Trabecular bone tissue strains in the healthy and osteoporotic human femur. *Journal of Bone and Mineral Research*, 18(10), 1781-1788.
- [75] Koivum aki, J. E., Thevenot, J., Pulkkinen, P., Kuhn, V., Link, T. M., Eckstein, F., & J ams a, T. (2012). Cortical bone finite element models in the estimation of experimentally measured failure loads in the proximal femur. *Bone*, 51(4), 737-740.



APPENDIX

Codes for calculating material properties and cortical thickness in MATLAB

```
info=dicominfo('dicomfilename');
space=info.PixelSpacing;
perareapixel=space(1)*space(2);
clear c
for i=1:512           %matrix size
    for j=1:512       %matrix size
        %converting HU unit from Dicom Image
        HU = Gray_Value * slope + intercept
        %(From dicominfo Rescale Slope=1, Rescale
Intercept=-1024)
        a(i,j)=a(i,j)-1024;
%HARP et. al.(1994) p = 7.69*10^-4 x QCT No.(HU) + 1.028
(p=apparent density)
        b(i,j)=(7.69*(10^-4))*a(i,j)+1.028;
        %Schaffle et. al.(1988) E = 0.09p^7.4
        if b(i,j)<=1.54
            b(i,j)=0.06+0.09*b(i,j)*b(i,j);
        end
        if b(i,j)>1.54
            b(i,j)=0.09*b(i,j)^7.4;
        end
        %Thresholding separate bone from soft tissue
        if a(i,j)<=226 %226 is the threshold value
            a(i,j)=-1024;
        end
    end
end
% for mean HU unit on cortical bone
s=0;
t=0;
for k=(selected areaX):(selected areaY)
    for j=(selected areaX): (selected areaY)
        t=b(j,k)+t;
        s=s+1;
    end
end
mean=t/s;
%average HU in the selected area
figure(MeanHU)
```

```

imshow(a, []);
x = uint16(getrect);
axis on
g=1;
h=1;
for i=x(2):(x(2)+x(4))
    h=1;
    for j= x(1):(x(1)+x(3))
        c(g,h)=a(i,j);
        h=h+1;
    end
    g=g+1;
end
imshow(c, [])
x =getline;    %calculating cortical thickness
r=edge(a, 'Roberts');
dis=(sqrt(abs(x(1,1)-x(2,1))^2+abs(x(1,2)-x(2,2))^2));
thickness=dis*space(1)

```

Codes material properties in ANSYS Apdl for two elements

```

! MATERIALS
MP,EX,1,X(Pa)           %Elastic Modulus for first element
MP,DENS,1,Y(g/cm3)    %Density for first element
MP,PRXY,1,Z            %Poisson's ratio for first element
MP,EX,2,A              %Elastic Modulus for second element
MP,DENS,2,B            %Density for second element
MP,PRXY,2,C            %Poisson's ratio for second element
MPCHG,(related element number),1 %assignment of material
    properties to elements
MPCHG,(related element number),2 %assignment of material
    properties to elements
END

```

CURRICULUM VITAE

Name Surname : Samet ÇIKLAÇANDIR
Place and Date of Birth : Kayseri, 29 January 1991
Address : Çiğli/İzmir
Email : samet.cikla@gmail.com
Work Experience : Research Assistant
(Izmir Katip Celebi University, 2016 -...)



EDUCATION :

B.Sc. : 2015, Erciyes University, Electrical and Electronics Engineering
B.Sc. : 2015, Erciyes University, Biomedical Engineering
A.S. : 2016, Anadolu University, Management of Health Institutions

Conference Papers

Çizmecioğulları, S., Mihçin, Ş., Çıklaçandır, S., Azizi, E., Akan, A. (2018). A novel methodology on evaluation of upper extremity motor functions. *9th International Biomechanics Conference* (pp. 384-386).

Çıklaçandır, S., Aygün, A. B. (2018). Electroporation Technique in Tumor Treatment and Electronic Design of an Electroporator Device. *First International Technological Sciences and Design Symposium*.

Çıklaçandır, S. (2018). Printing of Radiological Images in 3D Printer and Applications of Biomedical Engineering. *First International Technological Sciences and Design Symposium*.

Çıklaçandır, S. (2018). Finite Element Modelling for Acetabular Bone. *Second International Students Science Congress* (pp. 97).

Çıklaçandır, S., İşler, Y. (2018). Design of a new mechanism in medical applications with laser. *26th Signal Processing and Communications Applications Conference (SIU)* (pp. 1-4). IEEE.

Çıklaçandır, S., Karabiber Cura, Ö., Kalafat, Y., CAN, F. C. (2017). Design a Robot Insect Inspired by the Camouflage Characteristics of the Leaf Insect. *International Conference on Engineering Technologies (ICENTE'2017)* (pp. 668-671).

Çıklaçandır, S., İşler Y. (2017). System design for entertainment based rehabilitation of the upper extremity. *Tıp Teknolojileri Kongresi (TIPTEKNO'2017)* (pp. 364-367).

Mülayim, N., Çıklaçandır, S., CAN, F. C., ŞAHİN, S. (2017). Low-Cost Real-Time Electromyography (EMG) Data Acquisition Experimental Setup for Biomedical Technologies Education. *International Conference on Research in Education and Science (ICRES)* (pp. 155-161).

Çıklaçandır, S., Mülayim, N., ŞAHİN S. (2017). Low Cost Real-Time Measurement of the ECG, SPO2 and Temperature Signals in the LabVIEW Environment for Biomedical Technologies Education. *International Conference on Research in Education and Science (ICRES)* (pp. 162-168).